A simple model for the emergence of relaxation-oscillator convection

FRANCISCO E. SPAULDING-ASTUDILLO [1] AND JONATHAN L. MITCHELL [1,2]

[1] *Department of Earth, Planetary, and Space Sciences, University of California, Los Angeles*
595 Charles E Young Dr E, Los Angeles, CA 90095, USA
[2] *Department of Atmospheric and Oceanic Sciences, University of California, Los Angeles*
520 Portola Plaza, Los Angeles, CA 90095, USA

ABSTRACT

Earth's tropics are characterized by quasi-steady precipitation with small oscillations about a mean value, which has led to the hypothesis that moist convection is in a state of quasi-equilibrium (QE). In contrast, very warm simulations of Earth's tropical convection are characterized by relaxation-oscillator-like (RO) precipitation, with short-lived convective storms and torrential rainfall forming and dissipating at regular intervals with little to no precipitation in between. We develop a model of moist convection by combining a zero-buoyancy model of bulk-plume convection with a QE heat engine model, and we use it to show that QE is violated at high surface temperatures. We hypothesize that the RO state emerges when the equilibrium condition of the convective heat engine is violated, i.e., when the heating rate times a thermodynamic efficiency exceeds the rate at which work can be performed. We test our hypothesis against one- and three-dimensional numerical simulations and find that it accurately predicts the onset of RO convection. The proposed mechanism for RO emergence from QE breakdown is agnostic of the condensable, and can be applied to any planetary atmosphere undergoing moist convection. To date, RO states have only been demonstrated in three-dimensional convection-resolving simulations, which has made it seem that the physics of the RO state requires simulations that can explicitly resolve the three-dimensional interaction of cloudy plumes and their environment. We demonstrate that RO states also exist in single-column simulations of radiative-convective equilibrium with parameterized convection, albeit in a different surface temperature range and with much longer storm-free intervals.

PLAIN-LANGUAGE SUMMARY

Earth's tropics are characterized by steady rainfall, indicating that moist convection is a continuous process. However, in simulations of very warm conditions, a form of episodic convection emerges that is characterized by short bursts of intense rainfall followed by longer rain-free intervals. We construct a simple model that represents convection as a heat engine, and use it to show that steady convection must break down in very warm conditions. We hypothesize that the essential condition for steady convection is the balanced conversion of heat into work, which is violated at high surface temperatures. We test our hypothesis against climate model simulations of increasing complexity - the first parameterizes convection and the second actually resolves it - and found that it accurately predicts when the steady climate state transitions to the episodic state. The simple model of convection isn't limited to Earth, and could be applied to planets with different atmospheric compositions. Finally, while it has seemed that episodic precipitation could only be obtained from model simulations that resolve convection, we've shown here that it can also occur in simpler climate models with parameterized convection.

1. INTRODUCTION

To investigate the nature of convective dynamics in moist planetary atmospheres under varying conditions, we often rely on numerical climate models. These models are differentiated by whether or not they resolve convective processes, which refers to vertical motion at the scale of individual clouds ("plumes"). Models that can resolve convection are known to simulate the climate more realistically, but can be computationally expensive to run over very large domains. In coarse-resolution climate models that simulate the three-dimensional structure of the atmosphere on regional or global scales, parameterizations are employed to represent the net ("bulk") effect of an ensemble of unresolved plumes that turbulently mix with the surrounding environment. The bulk-plume representation of convection relates the properties of the plume ensemble (consisting of numerous members of varying size and intensity) to the large-scale radiative forcing through the concept of quasi-equilibrium (QE; Arakawa & Schubert 1974; Emanuel 2001). QE is, by definition, a *hypothesis* that there exists a steady balance between generation and dissipation of kinetic energy in convecting atmospheres (Yano & Plant 2012). The QE hypothesis has been invoked successfully in various contexts, for example, to reveal the dynamics of mature hurricanes (Emanuel 1986, 2001), formulate scaling laws for the maximum intensity of convective storms (Emanuel & Bister 1996), derive analytical solutions for the large-scale tropical circulation (Neelin & Zeng 2000), and resolve the closure problem in the bulk-plume parameterization of convection (Arakawa & Schubert 1974).[1] Thus, while the precise range of states over which QE is valid remains unclear (Yano & Plant 2012), its utility in advancing conceptual understanding of moist convection is evident.

In the contemporary solar system, there are two planets with similar atmospheric compositions but distinct convective dynamics: Earth and Saturn's moon Titan. Their atmospheres are nitrogen-dominated, and each has a condensing component that participates in an important "hydrological" cycle, i.e. the condensable undergoes phase changes to form clouds and precipitation (Hörst 2017). Whereas the condensing component on Earth is obviously water, the atmosphere of Titan is so cold that methane (and to a lesser extent nitrogen) condenses (Mitchell & Lora 2016; Tokano 2017) while water is part of the icy bedrock of the Titan's surface (Griffith et al. 2003). The pattern of global-mean precipitation on Earth (Figure 1a) from the MERRA-2 global climate reanalysis and Titan (Figure 1b) from global simulations of Titan by Faulk et al. (2020) reveals important differences in their hydrological cycles. On Earth, global-mean precipitation is quasi-steady about a mean value with small oscillations (Figure 1a), suggesting that modern Earth has QE-type convection. On Titan, however, rain is the exception, rather than the rule (Figure 1b); storms erupt at semi-regular intervals with vigorous, short-lived rainfall of several centimeters per Earth day and extended dry spells in between (Battalio et al. 2022). The largest observed storms produce cloud cover up to 10% of Titan's disk, in contrast to most observations showing very little cloud cover (Griffith et al. 1998; Schaller et al. 2009). During these storms (Dhingra et al. 2019; Turtle et al. 2011b), Titan's surface is likely subject to fluvial erosion which carves out channels and valleys and discharges the sediments into alluvial fans (Perron et al. 2006; Hörst 2017; Faulk et al. 2017; Lewis-Merrill et al. 2022).

Where does this striking difference in surface precipitation originate? In this study, we take the first step towards answering that question by taking a holistic view of the role of moisture in radiative-convective processes. For completeness, we begin with some background on the physics of moist convection as it relates to convective storms. The temperature of a moist air parcel decreases less rapidly with height than a dry air parcel displaced from the same initial location because of latent heat release. If the moist parcel is displaced adiabatically[2] above its saturation level, then it usually becomes warmer than the sub-saturated environment in which it is embedded, and therefore accelerates upward due to buoyancy,[3] condensing moisture along its path. The vertical integral of buoyancy B (m/s^2) along the upward trajectory of an adiabatic parcel can be decomposed into the meteorological quantities known as convective available potential energy (CAPE; J kg^{-1}) and convective inhibition (CIN; J kg^{-1}):

$$\int_0^{\text{LNB}} B\,dz = \text{CAPE} - \text{CIN}, \tag{1}$$

where

$$\text{CAPE} = \int_{\text{LFC}}^{\text{LNB}} B\,dz \ \text{ and } \ \text{CIN} = -\int_0^{\text{LFC}} B\,dz \tag{2}$$

---

[1] The definition of quasi-equilibrium has varied over time and between contexts, as is elegantly described in a review article by Yano & Plant (2012).

[2] An adiabatic parcel does not exchange mass or heat with its surroundings.

[3] The low molecular weight of water vapor on Earth and methane vapor on Titan relative to the dry background gases (Seidel & Yang 2020; Mitchell & Lora 2016) lends additional buoyancy to moist parcels of air (Yang & Seidel 2020).
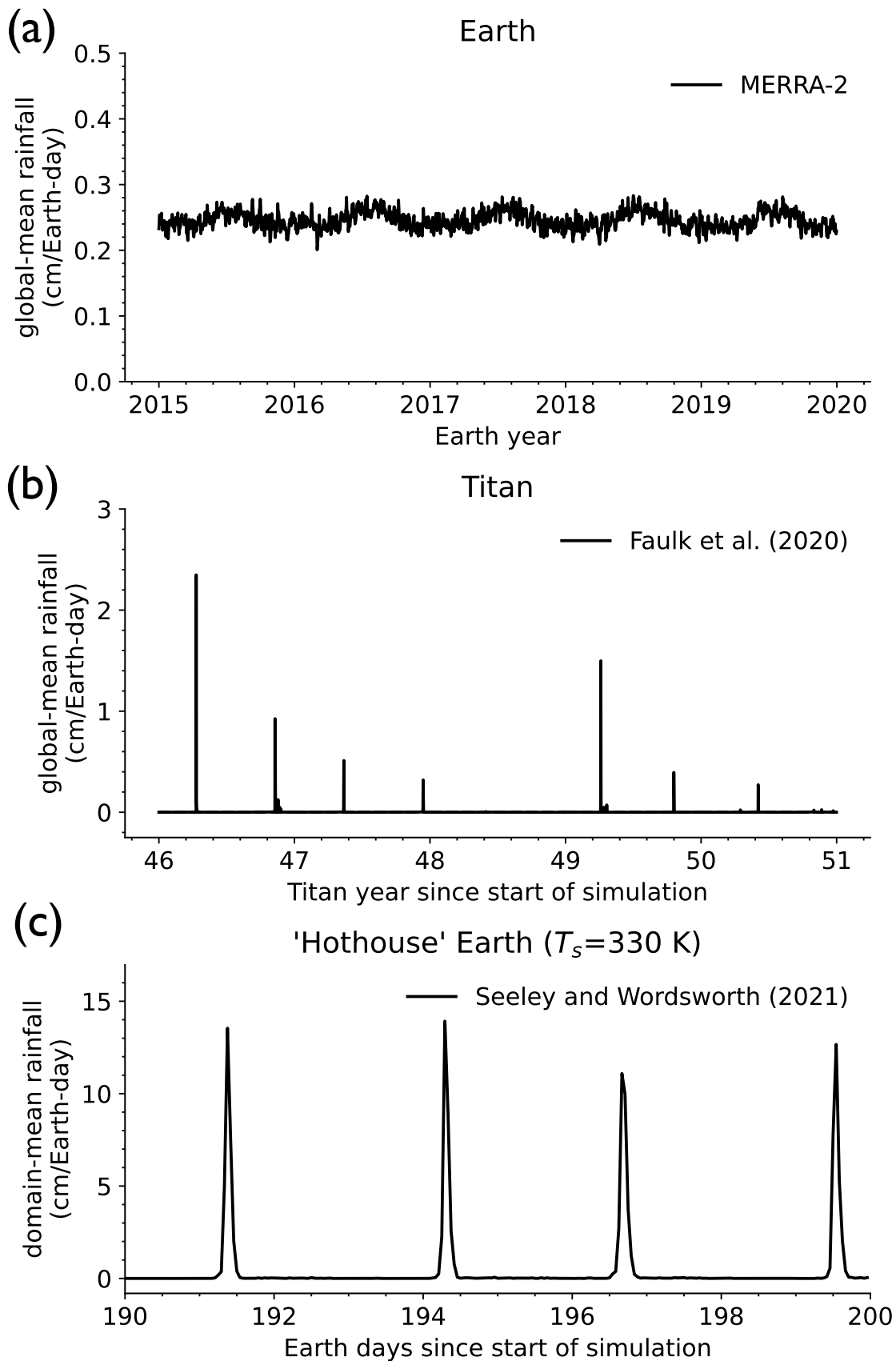
Figure 1. Comparison of global-mean precipitation on (a) Earth from the MERRA-2 Earth climate reanalysis (Gelaro et al. 2017) and (b) Titan from Titan Atmospheric Model simulations with best-fit land surface hydrology from Faulk et al. (2020), respectively. In (c), we show the domain-averaged precipitation in convection-resolving model aquaplanet simulations of the "Hothouse Earth" at a fixed surface temperature of 330 K from Seeley & Wordsworth (2021a).

are both expressed as positive values, LFC is the level of free convection, and LNB is the level of neutral buoyancy. Equation 1 represents the net work done to lift the adiabatic parcel from the surface to the LNB, and can be positive or negative. CAPE is an important meteorological quantity because it represents the maximum intensity of convective storms and is, for example, correlated with the frequency distribution of lightning flashes on Earth (Romps et al. 2018). CIN can be thought of as the energetic barrier to convection. In the global-mean, CAPE − CIN > 0 on Earth (Riemann-Campe et al. 2009) and there is some evidence to suggest that CAPE − CIN < 0 on Titan (Battalio et al. 2022). Given our interest in the maximum possible amount of work done by the climate system, we approximate the net vertical integral of buoyancy (Equation 1) as CAPE for the remainder of this study. Neglecting CIN could be a poor assumption in, for example, hydrogen atmospheres where the vapor phase of the condensing substance is significantly heavier than the dry background gas. CAPE measures the positive buoyancy that is generated by the absorption of solar radiation at the surface and emission of planetary radiation to space in the troposphere, and represents the "fuel" for thunderstorms. Coincidentally, regions of Titan with elevated near-surface humidity (∼60%) have similar values of CAPE to the modern-day tropics of Earth (Riemann-Campe et al. 2009; Griffith et al. 2008; Tokano et al. 2006; Barth & Rafkin 2007; Seeley & Wordsworth 2023), indicating the potential for intense storms and rainfall.

It has recently come to light that there is an emergent *dynamical similarity* between contemporary Titan and a hotter Earth (Figure 1b,c). The key discovery, in this case, was made by Seeley & Wordsworth (2021a) in a study of Earth's tropical clouds and precipitation, in which the authors incrementally increased the surface temperature in a convection-resolving model. At surface temperatures above 320 K, they discovered a "hothouse" climate state with a new mode of convection undergoing relaxation oscillations. The convective oscillations produced deluges lasting a few hours that then repeated every few days (Figure 1c). Unlike modern Earth, hothouse (often referred to as "moist greenhouse") climate simulations have radiative heating in the lower troposphere (Wolf & Toon 2015). Seeley & Wordsworth (2021a) hypothesized this lower-tropospheric radiative heating (LTRH) is a necessary condition for the RO state. LTRH occurs in hothouse climates because of the thermodynamic and radiative properties of water vapor. Around 320 K, the "water vapor window" - a spectral region over which the present-day atmosphere is transparent to infrared radiation - closes (Pierrehumbert 2010; Koll & Cronin 2018), which prevents the lower atmosphere from directly cooling to space (Wolf & Toon 2015). Seeley & Wordsworth (2021a) tested the LTRH hypothesis by carrying out a series of experiments with fixed radiative cooling profiles with and without LTRH. In cases with imposed LTRH, RO states emerged at much lower temperatures close to the modern-day tropics (∼290 K). In cases without LTRH, no RO states emerged. Two subsequent studies found that the RO state can emerge even in the absence of LTRH (Dagan et al. 2023; Song et al. 2024). Given the available evidence, LTRH is not a necessary condition for RO emergence, though it can support it.

There is a consensus among the aforementioned studies that water vapor plays an important role in the emergence of RO convection at high temperatures on Earth. In what follows, we explore the nature of that role. In QE convection, kinetic energy is generated and dissipated in the atmosphere at equal rates, conceivably leading to steady precipitation. Since the RO state is, by definition, non-steady, it suggests that we may conceive of the QE-to-RO transition as a *breakdown of quasi-equilibrium*. To look for a breakdown of QE convection with increasing surface temperature (and/or, as we will see, moisture content), what is needed is a plausible model of QE convection. Since the atmosphere is a compressible system, parcels/plumes exchange energy with the environment through heat exchange and work, the simplest QE model of convection is that of a heat engine (Rennó & Ingersoll 1996; Emanuel & Bister 1996) defined in the traditional way as any closed system that converts heat into work at some thermodynamic efficiency. In the context of an atmosphere, the work done by the convective heat engine is known as CAPE and heat is transferred to and from the system in the form of radiation (Arakawa & Schubert 1974; Emanuel 1986).

The dynamical similarity of Titan and the hothouse Earth (Figure 1a,c) could point to an underlying physical mechanism that is general to both planets, and their example motivates us to search for an explanation that is inclusive of both radiative and convective processes. A heat engine theory of convection would be agnostic of the atmospheric composition and the condensing substance. For this reason, it is an ideal framework to compare the atmospheres of Earth and Titan. While a goal for future work is to establish whether the theory can explain Titan's bursty methane precipitation (Figure 1b), the specific aim of this study is to apply the theory to Earth.

2. THEORY

The QE state is characterized by a steady balance between the generation of CAPE by radiation and its conversion into kinetic energy - i.e., convective motion. The RO state is clearly not steady, however we hypothesize that exploring
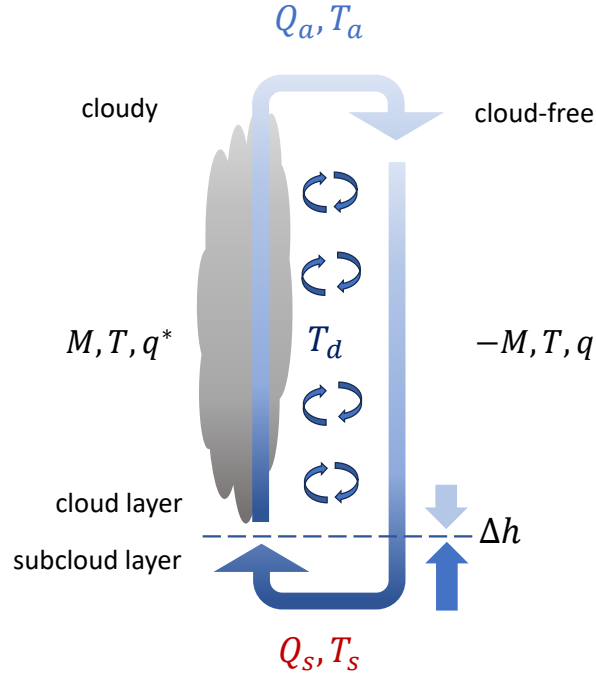
Figure 2. Schematic illustration of the zero-buoyancy heat engine model of convection based on Emanuel & Bister (1996) and Romps (2016). Radiation is absorbed by the surface at warm temperature T_s at a rate Q_s and emitted by the atmosphere at the cold temperature T_a at a rate Q_a. The mass flux M is assumed to be constant with height and equal in magnitude in ascending cloudy and descending cloud-free regions, which are permitted to turbulently mix. The rate of work is $M \times \mathrm{CAPE}$. Heat is converted into work at a thermodynamic efficiency η that is a ratio of the temperatures at which irreversible frictional dissipation occurs (T_d) and radiation is absorbed and emitted. In the zero-buoyancy approximation, cloudy regions and cloud-free regions have the same temperature T but different specific humidities at each height. In statistical equilibrium, mixing equal parts of air between the cloud layer and subcloud layer implies a net upward transport of moist static energy (Δh).

the conditions in which the steady, QE state is valid can illuminate the mechanisms that lead to the transition from QE to RO convection. First, we construct a quasi-equilibrium model of a convective heat engine (Section 2.1; Emanuel & Bister 1996) in which entraining clouds have zero-buoyancy relative to their local environment (Section 2.2; Singh & O'Gorman 2013; Romps 2016). Second, we demonstrate that QE-type convection is inconsistent with the energetic requirements of radiative-convective equilibrium when the surface is sufficiently warm and/or humid (Section 2.3). Thus, we predict that RO-type convection emerges in warm and humid conditions. A detailed list of the symbols, constants, and acronyms introduced in this section is given in Appendix A.

2.1. *Theory 1: convection as a heat engine*

Here, we summarize a quasi-equilibrium model of convection developed by Emanuel & Bister (1996) and others (Rennó & Ingersoll 1996; Pauluis & Held 2002a). We begin with the entropy budget of the climate system (defined as the surface and the atmosphere) in statistical equilibrium as commonly written (e.g., Pauluis & Held 2002a; Singh & O'Neill 2022):

$$\dot{S}_{rad} + \dot{S}_{irr} = 0, \tag{3}$$

where $\dot{S}_{rad} < 0$ is the entropy change associated with radiative processes and $\dot{S}_{irr} > 0$ is the entropy change associated with irreversible processes within the climate system. By convention, time rates of change of entropy have units of W K^{-1}. Since Earth receives low entropy energy from the sun and releases high entropy energy to space, radiative processes represent a sink of entropy (Singh & O'Neill 2022). Dry processes such as dissipation of convective turbulence and moist processes such as hydrometeor sedimentation, phase changes, and vapor diffusion irreversibly increase the entropy of the climate system (Pauluis & Held 2002a). In a dry atmosphere, the dominant contributor to entropy generation in $\dot{S}_{irr}$ is frictional dissipation of convective turbulence (Singh & O'Neill 2022). Although Earth's atmosphere is not dry, frictional processes remain a major source of dissipation because of hydrometeor drag (Pauluis

6

& Held 2002a; Singh & O'Gorman 2016). In what follows, we assume that the dominant source of entropy is frictional dissipation ($\dot{S}_d$; W K^{-1}), which should be understood as referring to both convective turbulence and hydrometeor drag. This key assumption of the heat engine model simplifies the entropy budget and will lead us to a solution for the equilibrium mass flux. The relative importance of frictional dissipation in the entropy budget over a range of surface temperatures was recently explored (Singh & O'Gorman 2016), where it was shown to account for approximately 50% of the total entropy generation at 305 K and increase with further surface warming. Some caveats of our approach are addressed in Section 5 and at greater length by several preceding studies (Singh & O'Neill 2022; Pauluis & Held 2002a; Emanuel 1986). The spatially-resolved flux of radiation at the surface is $\tilde{F}_s(x, y)$ (W m^{-2}), so the rate of energy transfer to the surface by radiation (W) is

$$Q_s = \int_A \tilde{F}_s, \tag{4}$$

where $\int_A = \int dx\, dy$ denotes an integral over the horizontal area of the system. Similarly, the spatially-resolved atmospheric cooling rate per unit mass is $\tilde{Q}_a(x, y, z)$ (W kg^{-1}). The rate of energy loss from the atmosphere by radiation (W) is

$$Q_a = \int_V \rho\, \tilde{Q}_a, \tag{5}$$

where p is pressure, ρ is density, g is gravity, and $\int_V = \int dx\, dy\, dz = -\int_A \int \frac{dp}{\rho g}$ is an integral over the system volume. Atmospheric cooling (F_a; W m^{-2}) balances surface heating (F_s; W m^{-2}) in equilibrium:

$$F_s + F_a = \frac{Q_s}{A} + \frac{Q_a}{A} = 0, \tag{6}$$

where A is the horizontal area of the system. Radiative processes are assumed to be thermodynamically reversible where absorption and emission occur at a mean temperature of T_s and T_a. The spatially-resolved rate of change of specific entropy associated with radiative processes (W kg^{-1} K^{-1}) is

$$\dot{s}_{rad} = \frac{\tilde{Q}_a}{T}. \tag{7}$$

The total rate of decrease in entropy of the system ($\dot{S}_{rad}$; W K^{-1}) is

$$\dot{S}_{rad} = \int_V \rho \dot{s}_{rad} = \frac{Q_a}{T_a} + \frac{Q_s}{T_s} = Q_a \left(\frac{1}{T_a} - \frac{1}{T_s} \right), \tag{8}$$

where

$$\frac{1}{T_a} = \frac{\int_V \rho \tilde{Q}_a / T}{\int_V \rho \tilde{Q}_a}. \tag{9}$$

Invoking quasi-equilibrium, we assume that the rates of kinetic energy generation ($\dot{W}$; W) and dissipation ($\dot{D}$; W) are equal. By definition, $\dot{W}$ is also the rate of work. It can be shown that, in statistical equilibrium, these processes are balanced in the volume integral of the "kinetic energy equation" (i.e., the equation describing the time rate of change of kinetic energy per unit volume; Emanuel & Bister 1996; Pauluis & Held 2002a):

$$\dot{W} - \dot{D} = 0, \tag{10}$$

where

$$\dot{W} = \int_V -v \cdot \nabla p \text{ and } \dot{D} = -\int_V \rho f \cdot v. \tag{11}$$

Here, v is the velocity and f is the frictional force per unit mass. The spatially-resolved rate of change of specific entropy associated with frictional dissipation (W kg^{-1} K^{-1}) is

$$\dot{s}_d = -\frac{f \cdot v}{T}. \tag{12}$$

Frictional dissipation is an irreversible source of entropy ($\dot{S}_d$; W K^{-1}); assuming it occurs at a mean temperature T_d,

$$\dot{S}_d = \int_V \rho \dot{s}_d = -\frac{1}{T_d} \int_V \rho f \cdot v = \frac{\dot{D}}{T_d} = \frac{\dot{W}}{T_d}. \tag{13}$$

Following Pauluis & Held (2002a), we can now re-write the entropy budget (Equation 3) first by defining a new variable $\Delta \dot{S} = \dot{S}_{irr} - \dot{S}_d$ to be all irreversible sources of entropy *except* frictional dissipation and second by substituting $\dot{S}_{rad}$ (Equation 8) and $\dot{S}_d$ (Equation 13):

$$Q_a \left(\frac{1}{T_a} - \frac{1}{T_s} \right) + \frac{\dot{W}}{T_d} + \Delta \dot{S} = 0. \tag{14}$$

Re-arranging this expression and solving for the rate of work, we find

$$\dot{W} = -Q_a T_d \left(\frac{1}{T_a} - \frac{1}{T_s} \right) - T_d \Delta \dot{S} \approx -\eta Q_a, \tag{15}$$

where

$$\eta = T_d \left(\frac{1}{T_a} - \frac{1}{T_s} \right) \tag{16}$$

is the efficiency of the heat engine when frictional dissipation is the only source of entropy generation. Equation 15 nicely demonstrates that the other sources of entropy $\Delta \dot{S}$ reduce the amount of work that can be performed by the heat engine. As a logical starting place, in the second step of Equation 15, we assume that $\Delta \dot{S} = 0$. Indeed, Pauluis & Held (2002a) point out that, in making this assumption, one is actually solving for the maximum rate of work that can be performed given the typical forcing on and state of the system. Emanuel & Bister (1996) show that to a good approximation

$$\dot{W} \approx \int_V MB, \tag{17}$$

where M is the mass flux (kg m^{-2} s^{-1}) and

$$B = g \frac{(\overline{\rho} - \rho)}{\rho} \tag{18}$$

is the buoyancy (m s^{-2}), $\overline{\rho}$ is the mean density of the system, and ρ is the spatially-resolved density of the working fluid (i.e. the parcel/plume); MB is the buoyancy flux (W m^{-3}). The above imply the rate of work is equal to the buoyancy flux. We can simplify Equation 17 as follows:

$$\int_V MB = \int_z \iint_{A_u} M_u B_u + \int_z \iint_{A_d} M_d B_d$$

$$\approx A_u M_u \int_z B_u + A_d M_d \int_z B_d$$

$$\approx A \times |M| \times \text{CAPE} \tag{19}$$

where A_u, A_d and M_u, M_d are the respective areas and mass fluxes of the updrafts and downdrafts. Together, they span the system area: $A_u + A_d = A$. In the first step, we decompose the volumetric integral over the system into updrafts and downdrafts. In the second step, we assume that the mass fluxes are constant (true, for example, in an adiabatic plume) and that buoyancy of updrafts and downdrafts is horizontally homogeneous.[4] Thus, the area integrals become trivial. Conservation of mass in statistical equilibrium requires that $M_u A_u = -M_d A_d$. In the case of dry convection, $A_u = A_d$ (Bjerknes 1938; Singh & O'Neill 2022) implying that $|M| = M_u = -M_d$ and, if updrafts and downdrafts do equal amounts of pressure work, $\int_z B_u = -\int_z B_d$. In the third step, we invoke the equal area assumption of updrafts and downdrafts (this is an, admittedly, poor assumption for moist convection) and neglect CIN. Thus, we arrive at our desired approximation for the buoyancy flux (Equation 19). CAPE is the convective available potential energy, i.e. the part of the potential energy that is available to convert to kinetic energy. Finally, by substituting $Q_a = F_a A$ (Equation 6) and Equation 19 into the simplified entropy budget (Equation 15), we arrive

---

[4] Buoyancy is approximately horizontally homogeneous in Earth's tropics (Sobel et al. 2001; Seidel & Yang 2020).

at

$$|M| \times \text{CAPE} = -\eta F_a \ . \tag{20}$$

The above equation can be thought of as representing a convecting atmosphere as a heat engine in quasi-equilibrium. The engine is heated at the rate $F_s = -F_a$ (positive values for heating), but is not perfectly efficient and therefore does work at a rate $|M| \times \text{CAPE}$. Solving for the mass flux implied by the convective heat engine,[5]

$$|M| = \frac{-\eta F_a}{\text{CAPE}} \ . \tag{21}$$

2.1.1. *The subcloud mass flux in radiative-convective equilibrium*

Following Emanuel & Bister (1996), we divide the system into a subcloud layer and a cloud layer. In the two-layer model, the cooling rate sums over both layers of the atmosphere:

$$F_a = F_{a,sc} + F_{a,cl} \tag{22}$$

The energy budget of the subcloud layer in radiative-convective equilibrium allows us to estimate the mass flux therein:

$$AF_s + AF_{a,sc} - (A_u M_{u,sc} h_{sc} + A_d M_{d,cl} h_{cl}) = 0$$
$$F_s + F_{a,sc} + |M_{sc}|(h_{cl} - h_{sc}) = 0. \tag{23}$$

Here, the subscript "sc" indicates the subcloud layer, the subscript "cl" indicates the cloud layer, and $h = c_p T + gz + Lq$ is the moist static energy (MSE). Therefore, $M_{u,sc}$ is the updraft mass flux from the sub-cloud layer and $M_{d,cl}$ is the downdraft mass flux from the cloud layer. To obtain Equation 23, we invoke mass conservation in statistical equilibrium ($A_u M_{u,sc} = -A_d M_{d,cl}$) and the equal area assumption of updrafts and downdrafts where $A_u + A_d = A$, implying that $|M_{sc}| = M_{u,sc} = -M_{d,cl}$ where M_{sc} is the sub-cloud mass flux. Mixing equal parts of air between the two layers implies a net upward transport of MSE, though this is conditional upon MSE decreasing with height. Following Emanuel & Bister (1996), we assume that the air parcels representative of the sub-cloud layer originate near the surface and those representative of the cloud layer originate near the tropospheric minimum in MSE,[6] and are exchanged across the lifting condensation level (LCL). If the parcels conserve their MSE, the two-layer MSE difference is

$$\Delta h = h_{sc} - h_{cl}$$
$$= \Delta(c_p T) + \Delta(gz) + \Delta(Lq)$$
$$\approx c_p(T_s - T_{min}) + g(z_s - z_{min}) + L(q_s - q_{min}) \tag{24}$$

where the subscript "s" indicates the near-surface, the subscript "min" indicates the tropospheric minimum in MSE, $\Delta(c_p T) + \Delta(gz)$ is the dry static energy difference, and $\Delta(Lq)$ is the latent energy difference. Substituting $F_s = -F_a$ (Equation 6) and Equation 22 into the sub-cloud energy budget (Equation 23), we solve for the mass flux from the sub-cloud layer:

$$|M_{sc}| = -\frac{F_{a,cl}}{\Delta h} \approx -\frac{F_a}{\Delta h} \tag{25}$$

It is clear that the role of convection in radiative-convective equilibrium is to re-distribute latent and sensible heat. Here, we have assumed that cooling rates are small in the subcloud layer such that $F_{a,cl} \approx F_a$.[7] The approximate form of $|M_{sc}|$ (Equation 25) follows from this simplification. $|M_{sc}|$ can be interpreted as the mass flux in radiative-convective equilibrium. Mass continuity requires $|M_{sc}| \approx |M|$.

2.2. *Theory 2: convection in a zero-buoyancy world*

As demonstrated by Singh & O'Gorman (2013), the vertical integral of cloud buoyancy taken relative to the clear-sky environment in convection-resolving model simulations is near zero. Based on this insight, they proposed a conceptual model of convection in which clouds are exactly neutrally-buoyant with respect to their environment.

---

[5] Equation 20 is typically utilized as a way of estimating CAPE (Rennó & Ingersoll 1996; Emanuel & Bister 1996).

[6] The tropospheric minimum in MSE tends to be near the emission level, so one would obtain similar results using an air parcel at T_a to represent the cloud layer instead.

[7] The intriguing possibility for lower-tropospheric radiative heating ($F_{a,sc} > 0$) to violate quasi-equilibrium could be explored in future work through Equations 9, 22, and 25.

This assumption about typical cloud buoyancies is known as the *zero-buoyancy approximation*. Romps (2014, 2016) introduced an analytical model of zero-buoyancy convection, in which the steady-state humidity and temperature fields of the atmosphere are determined by the turbulent interaction between ascending cloudy air and descending environmental air. The requirement that entraining clouds are neutrally buoyant with respect to the environment does not imply zero CAPE, which specifically depends on the buoyancy of a non-entraining parcel/plume relative to the mean environment. To see this, consider the formal definition of CAPE (Equation 2). Equations 2 and 18 tell us that two variables are required to estimate CAPE: the mean density $\overline{\rho}$ and the non-entraining parcel/plume density ρ. It is straightforward to calculate ρ given surface boundary conditions. What is needed to find CAPE, therefore, is a plausible environmental profile of $\overline{\rho}$. The environmental $\overline{\rho}$ is equal to the density of an *entraining* cloud in the zero-buoyancy approximation, and this is what allows a closed-form model of CAPE. The zero-buoyancy model of CAPE has been validated against convection-resolving model simulations (Romps 2016; Seeley & Wordsworth 2023).

Below, we re-derive the zero-buoyancy theory of CAPE (Romps 2016) in order to estimate its dependence on surface temperature and moisture. We begin by approximating the saturation specific humidity as

$$q^* = \frac{R_a}{R_v}\frac{e^*}{p}, \tag{26}$$

where R_a is the specific gas constant of environmental air (everywhere assumed to be that of dry air) and p is the total air pressure. Taking the vertical derivative of the natural log of e^* (and using the definition of the lapse rate $\Gamma = -\partial_z T$), we obtain

$$\partial_z e^* \;= \partial_T e^* \partial_z T = -\frac{Le^*\Gamma}{R_v T^2},$$

$$\partial_z \ln e^* = -\frac{L\Gamma}{R_v T^2}. \tag{27}$$

The vertical derivative of the natural log of p is obtained from hydrostatic balance and the ideal gas law:

$$\partial_z \ln p = -\frac{g}{R_a T}, \tag{28}$$

where g is gravity. Taking the vertical derivative of the natural log of q^* and plugging in Equations 27 and 28, we obtain

$$\partial_z \ln q^* = \partial_z \ln e^* - \partial_z \ln p,$$

$$= \frac{g}{R_a T} - \frac{L\Gamma}{R_v T^2} = -\gamma. \tag{29}$$

where γ is the moisture lapse rate (kg kg^{-1} m^{-1}). The tropospheric moisture budget is obtained from the bulk-plume equations for convection in steady-state:

$$\partial_z M = e - d - c, \text{ where } e = \varepsilon M \text{ and } d = \delta M, \tag{30}$$

$$\partial_z (Mq^*) = eq - dq^* - c, \text{ and} \tag{31}$$

$$-\partial_z (Mq) = dq^* - eq + (1-\mathrm{PE})c. \tag{32}$$

M is the convective mass flux (kg m^{-2} s^{-1}), e and d are the turbulent entrainment and detrainment rates (kg m^{-3} s^{-1}) in which ε and δ are fractional mixing efficiencies (m^{-1}), and c is the condensation rate (kg m^{-3} s^{-1}). PE is the precipitation efficiency, defined as the fraction of condensates generated in updrafts at each height that are not re-evaporated in the environment. Per this definition, the gross evaporation is $(1-\mathrm{PE})c/M$ and the gross condensation minus gross evaporation is $\mathrm{PE}c/M$.[8] We make the following assumptions. The condensates not re-evaporated at each level ($\mathrm{PE}c/M$) are immediately removed from the convective plume. The gross condensation represents a small fraction of the total updraft mass ($\partial_z M >> c$). Invoking the latter assumption in Equation 30 gives

$$\partial_z M = e - d$$

$$= (\varepsilon - \delta)M. \tag{33}$$

---

[8] Re-evaporation in the atmosphere is an irreversible source of entropy (Emanuel 2001) that is neglected in the heat engine model (Emanuel & Bister 1996).

10

Expanding Equation 31 with the chain-rule and solving for $\partial_z q^*$ (using Equation 33), we obtain

$$\partial_z q^* = \varepsilon(q - q^*) - \frac{c}{M}. \tag{34}$$

Doing the same to Equation 32 to find $\partial_z q$,

$$-\partial_z q = \delta(q^* - q) + (1 - \mathrm{PE})\frac{c}{M}. \tag{35}$$

The relative humidity is approximated as $\mathrm{RH} = q/q^*$. Rearranging for q,

$$q = \mathrm{RH}q^*, \tag{36}$$

and taking the vertical derivative of both sides, we obtain

$$\partial_z q = q^* \partial_z \mathrm{RH} + \mathrm{RH}\partial_z q^*. \tag{37}$$

We assume that vertical variations in RH are much smaller than those in specific humidity ($\partial_z \mathrm{RH} << \partial_z q^*$), as is generally the case in Earth's troposphere. Invoking this assumption in Equation 37 gives

$$\partial_z q = \mathrm{RH}\partial_z q^*. \tag{38}$$

Using Equations 29, 36, and 38 to re-write Equations 31 and 32, we obtain

$$-\gamma q^* = \varepsilon(\mathrm{RH} - 1)q^* - \frac{c}{M} \text{ and} \tag{39}$$

$$\mathrm{RH}\gamma q^* = \delta(1 - \mathrm{RH})q^* + (1 - \mathrm{PE})\frac{c}{M}. \tag{40}$$

To solve for RH, we substitute $\frac{c}{M}$ from Equation 39 into Equation 40.

$$\mathrm{RH} = \frac{\delta + (1 - \mathrm{PE})\gamma - (1 - \mathrm{PE})\varepsilon}{\delta + \gamma - (1 - \mathrm{PE})\varepsilon} \tag{41}$$

We invoke the zero-buoyancy assumption (Singh & O'Gorman 2013) to define the MSE (h) of the environment and the plume.

$$h = c_p T + gz + Lq \tag{42}$$
$$h^* = c_p T + gz + Lq^* \tag{43}$$

In the zero-buoyancy assumption, ascending plumes are neutrally buoyant with respect to their environment. Strictly speaking, this means that their *virtual* temperatures are the same. When virtual effects are neglected, as is done here, the plume and the environment possess the same temperature T such that their moist static energies differ only by the differences in their specific humidities. c_p is the specific heat of the atmosphere (assumed to be dry air, c_{pa}). Next, taking the vertical derivative of h^* (and using $\Gamma = -\partial_z T$, $\partial_z q^* = -\gamma q^*$, and Equation 29),

$$\partial_z h^* = -c_p \Gamma + g - L\gamma q^*$$
$$= g\left(1 + \frac{Lq^*}{R_a T}\right) - \Gamma\left(c_p + \frac{L^2 q^*}{R_v T^2}\right). \tag{44}$$

It follows from Equation 30 that the vertical change in MSE flux with height for an entraining plume is

$$\partial_z(Mh^*) = (\varepsilon h - \delta h^*)M. \tag{45}$$

Using the chain rule to solve for $\partial_z h^*$ (and substituting Equations 33, 42, and 43):

$$\partial_z h^* = \varepsilon(h - h^*)$$
$$= \varepsilon(q - q^*)L$$
$$= \varepsilon(\mathrm{RH} - 1)Lq^*. \tag{46}$$

To connect with the heat engine model, we assume that M is constant with height. By Equation 33, this implies that $\varepsilon = \delta$. Next, we assume that RH and PE are also invariant. A consequence of this assumption is that, by Equation 41, the ratio of ε and γ is a constant. Following Romps (2016), we combine the preceding constants into a "bulk-plume parameter" that is, by design, invariant with height:

$$a = \text{PE}\frac{\varepsilon}{\gamma}. \tag{47}$$

The next step is to express the system of equations in the zero-buoyancy model in terms of this bulk-plume parameter. Relative humidity (Equation 41) simplifies to

$$\text{RH} = \frac{1 + a - \text{PE}}{1 + a}. \tag{48}$$

A trivial re-arrangement of Equation 47 yields ε:

$$\varepsilon = \frac{\gamma a}{\text{PE}} \tag{49}$$

Substituting ε (Equation 49) and RH (Equation 48) into Equation 46,

$$\partial_z h^* = -\frac{a}{1 + a}\gamma L q^*. \tag{50}$$

Equating the expressions for the vertical gradient in saturation moist static energy (Equations 44 and 50) and solving for Γ,

$$\Gamma = \frac{g}{c_p}\left[\frac{1 + a + q^* L/(R_a T)}{1 + a + q^* L^2/(c_p R_v T^2)}\right]. \tag{51}$$

Equation 51 is the temperature lapse rate set by entraining convection and is accurate when the water vapor mixing ratio is less than one. By neglecting virtual effects, the convective available potential energy (Equation 2) in steady-state becomes

$$\text{CAPE} \approx \int_{\text{LFC}}^{\text{LNB}} g\frac{T - \overline{T}}{\overline{T}}dz, \tag{52}$$

where T is the temperature of a pseudo-adiabatic parcel and $\overline{T}$ is the mean environmental temperature. We obtain T and $\overline{T}$ by integrating the zero-buoyancy model vertically with $a = 0$ and $a \geq 0$, respectively. PE and a are prescribed constants. Given the precipitation efficiency and mean relative humidity from simulations, an appropriate input value of a can be diagnosed via Equation 48. a controls the moist coupling between convective plumes and environmental air (for further discussion, see Seeley & Wordsworth 2023). For non-entraining convection ($a = 0$), Γ equals the moist adiabatic lapse rate, Γ_m. As a increases, the tighter coupling between the entraining plume and the environment forces Γ apart from Γ_m (Seeley & Wordsworth 2023), permitting more CAPE in steady-state.

The zero-buoyancy model shows a peak in CAPE at intermediate surface temperatures (Figure 3a) because the temperature difference $\Delta T = T - \overline{T}$ (Equation 52) between adiabatic parcels and the mean environment becomes negligible when the saturation specific humidity approaches the extremes of zero or one. Since CAPE is directly proportional to ΔT, CAPE is near zero in both the dry and moist limits, with a maximum in between (Seeley & Wordsworth 2023). From a more technical perspective, Singh & O'Gorman (2013) explain that ΔT is inversely proportional to a pseudo-heat capacity $\beta = c_p + L^2 q^*/(R_v T^2)$. Since the heat capacity of dry air is held constant, $1/\beta$ primarily decreases with increasing moisture. Combining these insights, Romps (2016) demonstrate that CAPE starts to decrease with rising surface temperatures when $\beta > 2c_p$ throughout the troposphere, meaning further increases in moisture reduce ΔT.

To summarize, the system of equations for a convecting atmosphere in radiative-convective equilibrium under the zero-buoyancy approximation are q and q^*, γ, RH, Γ, and CAPE. The final forms of the equations assume that the convective mass flux, the relative humidity of the environment, and precipitation efficiency are constant with height. The thermodynamic constants and their units and values in "Earth-like" and "Titan-like" conditions are given in Appendix A and are also assumed to be constant with height.
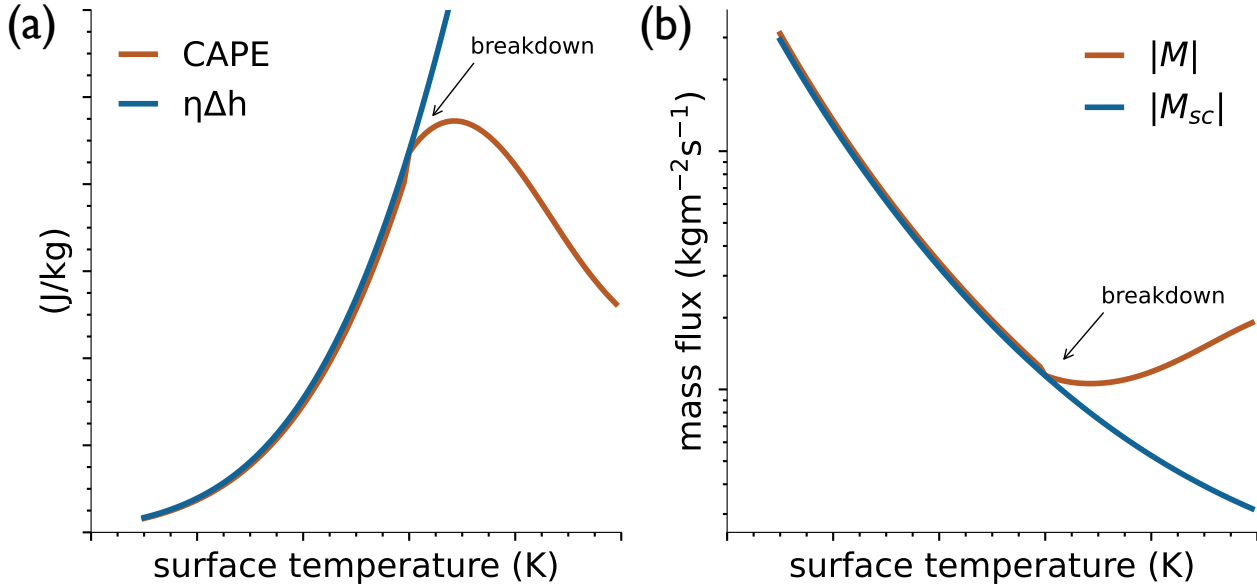
Figure 3. Schematic illustration of the breakdown of convective quasi-equilibrium with increasing temperature. (a) Comparison of convective available potential energy (CAPE; J kg^{-1}) and the vertical MSE difference (Δh; J kg^{-1}) times the heat engine efficiency η as a function of surface temperature. (b) Comparison of the heat engine mass flux $|M| \propto 1/$CAPE and the subcloud mass flux $|M_{sc}| \propto 1/\Delta h$ as a function of surface temperature. Quasi-equilibrium breaks down when $\eta\Delta h >$ CAPE, as this indicates $|M_{sc}| < |M|$.

2.3. The equilibrium condition

Emanuel & Bister (1996) equate $|M|$ (Equation 21) and $|M_{sc}|$ (Equation 25) to derive an expression for CAPE. This is clearly necessary for statistical equilibrium, in which there is no net vertical transport of mass. Doing so, we find that QE convection requires a conversion of the vertical MSE difference (Δh) into CAPE at an efficiency η:

$$|M| \approx |M_{sc}| \rightarrow \eta\Delta h \approx \text{CAPE}. \tag{53}$$

Henceforward, Equation 53 is called the *equilibrium condition*. To estimate CAPE and Δh, we instead use a zero-buoyancy model of convection (see Section 2.2). It's important to note that the CAPE predicted by the zero-buoyancy model represents a steady-state storage of buoyancy, not the rate of CAPE generation and destruction by radiation and convection.

We pose the following question: Is there a regime where $|M|$ and $|M_{sc}|$ don't equal one another, and if so, what does that imply about convection? In such a regime, QE convection would be incompatible with radiative-convective equilibrium. We argued previously that $|M| \propto 1/$CAPE (Equation 21) and $|M_{sc}| \propto 1/\Delta h$ (Equation 25), so any constraint on mass fluxes naturally applies to CAPE and Δh. This is depicted schematically in Figure 3. Of course, Δh can increase without restriction (up to the limit of a steam atmosphere) as moisture increases by the Clausius-Clapeyron relation (Figure 3a). This implies that $|M_{sc}|$ decreases monotonically (Figure 3b). However, convection in the zero-buoyancy model has a peak in CAPE at intermediate surface temperatures (Figure 3a; Seeley & Wordsworth 2023) due to the increasing influence of latent heat on the "effective" heat capacity of the troposphere (Romps 2016), implying a lower bound on $|M|$ but no upper bound (Figure 3b). If $|M| < |M_{sc}|$, the heat engine of the cloud layer would be over-driven, this would likely reduce CAPE, and the system would adjust to QE. This adjustment process implies $|M| \approx |M_{sc}|$ is a characteristic of QE, which is the condition invoked by others to constrain CAPE (Rennó & Ingersoll 1996; Emanuel & Bister 1996). Clearly, our theory also predicts $|M| > |M_{sc}|$ at surface temperatures above the threshold where $\eta\Delta h >$ CAPE (Figure 3b). In this case, the subcloud layer cannot meet the mass flux demand required of the cloud layer heat engine, the layers decouple, and the cloud is cut off from the moisture source – steady, QE convection cannot exist in this regime. Lacking convection, CAPE would build over time until $|M| \approx |M_{sc}|$, triggering convection. Our "QE-breakdown" hypothesis for the emergence of RO convection is simply:

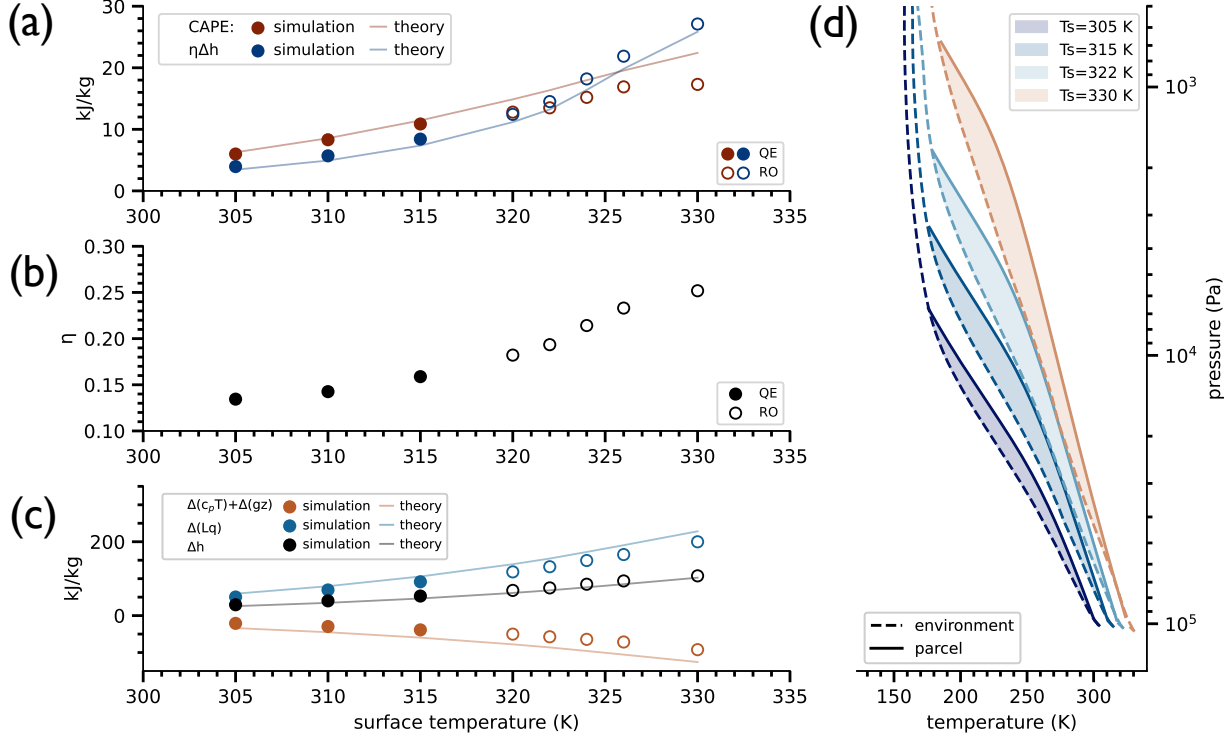Convection-resolving model simulations from Seeley and Wordsworth (2021)

Figure 4. (a) Comparison of convective available potential energy (CAPE; J kg^{-1}) and the vertical MSE difference (Δh; J kg^{-1}) times the heat engine efficiency η as a function of surface temperature. (b) Comparison of η (blue) with the maximum theoretical efficiency, η_{max}, as a function of surface temperature. (c) Dry $\Delta(c_p T)$ and moist $\Delta(Lq)$ contribution to the MSE difference of upward and downward plumes across the LCL as a function of surface temperature. (d) Temperature difference of the environment and an adiabatically-lifted surface parcel in the simulation, given as a proxy for the steady-state CAPE. In (a)-(c), circular markers are diagnosed values from the fixed sea surface temperature simulations of Seeley & Wordsworth (2021a).

$$\eta \Delta h > \text{CAPE}. \tag{54}$$

₄₀₆ 3. TESTING THE THEORY AGAINST CONVECTION-RESOLVING MODEL SIMULATIONS

₄₀₇ We now test the zero-buoyancy heat engine theory of convection against fixed surface temperature simulations from ₄₀₈ Seeley & Wordsworth (2021a) performed with the convection-resolving model DAM (Romps 2008). We use separate ₄₀₉ procedures to obtain estimates for η, Δh, and CAPE from the theory and from the simulations, which are described ₄₁₀ below. Some elements of the theory must be diagnosed from the simulations, so by "testing" we mean that we are ₄₁₁ establishing consistency between QE breakdown of the heat engine model and the onset of the RO state in simulations.

₄₁₂ To calculate the steady-state CAPE in the simulations as a function of surface temperature (Figure 4a), we use the ₄₁₃ standard formula that includes virtual effects (Equation 2). The temperature of the "adiabatic" parcel varies with ₄₁₄ height in accordance with the conservation of the sum of MSE and CAPE (i.e., MSE+CAPE; Romps 2015; Marquet ₄₁₅ 2016). We parameterize condensed water loss from the parcel as exponential decay over a length scale of 5 km following ₄₁₆ Seeley & Wordsworth (2023). The implementation of the MSE+CAPE parcel lifting method is detailed in Appendix ₄₁₇ C following Romps (2015).

₄₁₈ To obtain a theoretical prediction for CAPE, we initialize the zero-buoyancy model with the temperature and ₄₁₉ pressure of a near-surface parcel at the LCL. The precipitation efficiency (PE) and the relative humidity (RH) as a ₄₂₀ mass-weighted tropospheric mean are determined from the simulation. We diagnose the precipitation efficiency as the ₄₂₁ ratio of the surface precipitation rate (P_s; kg m^{-2} s^{-1}) to the vertically-integrated sink of water vapor associated with ₄₂₂ phase changes (SI; kg m^{-2} s^{-1}) following Sui et al. (2007):

$$\text{PE} = \frac{P_s}{\text{SI}}. \tag{55}$$

By substituting PE and RH into Equation 48, we obtain a self-consistent estimate for the bulk-plume parameter in the simulation:

$$a = \max\left(\frac{1 - \text{RH} - \text{PE}}{\text{RH} - 1}, 0\right). \tag{56}$$

a quantifies the strength of the coupling between entraining plumes and their environment, taking into account both entrainment and re-evaporation. The constraint that $a \geq 0$ follows from the requirement that $\text{RH} \geq 1 - \text{PE}$ (Romps 2014). When $a = 0$, $\text{RH} = 1 - \text{PE}$ and environmental temperatures follow the moist adiabat. For those interested, Figure 8b-d in Appendix B shows PE, RH, and a from the convection-resolving model of Seeley & Wordsworth (2021a). Representative parameter values of the quasi-equilibrium state in the convection-resolving model (RH = 0.82, PE = 0.27, and $a = 0.5$) are used to evaluate the zero-buoyancy model as a function of temperature. Figure 4a shows the theoretical and simulated CAPE. The simulated CAPE steadily increases in the convection-resolving model experiments of Seeley & Wordsworth (2021a) from 6 kJ/kg to 17 kJ/kg over the surface temperature range of 305-330 K. The growth in CAPE is explained by Figure 4d, which compares the environmental temperature to that of a surface parcel displaced adiabatically to the level of neutral buoyancy. CAPE is proportional to shaded area between the two curves in Figure 4d that represents the temperature difference between the environment and the parcel, where it can be seen that the size of the shaded area increases with surface warming in the simulations.

The heat engine efficiency η (Equation 16) depends on the mean temperature at which frictional dissipation occurs (T_d) and the mean inverse temperatures at which radiation is absorbed at the surface ($1/T_s$) and emitted from the atmosphere ($1/T_a$). The maximum efficiency of the convective heat engine (η_{max}; Figure 4b) would be achieved if frictional dissipation occurs only at the surface and the net emission level corresponds to the tropopause, $\eta_{max} = (T_s - T_{trp})/T_{trp}$, where T_{trp} is an assumed tropopause temperature of 200 K. T_s and T_{trp} clearly represent the warmest and coldest points of the system, respectively. Over the surveyed surface temperature range, η_{max} takes values between 52-65%. Rather than assuming the maximum efficiency, we make the reasonable assumption that most of the frictional dissipation occurs between the surface and the effective emission level such that $T_d = (T_s + T_a)/2$. Lacking a theory for the radiative cooling of the atmosphere (Q_a) to diagnose T_a (Equation 9), we instead obtain it from the model output of Seeley & Wordsworth (2021a), which yields our estimate for η with realistic radiation (Figure 4b). We find that T_a ranges from 258 K to 272 K (Figure 8a) in the simulations. Since the heat engine efficiency is sensitive to the radiation, we treat the simulation values as the "theoretical" prediction for η. The predicted efficiency is almost 15% at 305 K, and increases with surface warming up to 25% at 330 K. Raising the surface temperature drives more water vapor into the atmosphere, which increases radiative absorption at infrared and visible wavelengths. The spectral region over which the present-day atmosphere is transparent to infrared radiation (i.e., the water vapor window) begins to close at surface temperatures greater than 300 K, and becomes fully opaque at 320 K due to water vapor continuum absorption (Koll & Cronin 2018). Thus, the radiative properties of water vapor reduce T_a with surface warming above 320 K (Figure 8a), which along with increasing surface temperatures further increases η.

The vertical difference in MSE, Δh (Equation 24), dry static energy, $\Delta(c_p T) + \Delta(gz)$, and latent energy, $\Delta(Lq)$ are displayed in Figure 4c. Our method of evaluating Δh in the simulations and the theory is described in Section 2.1.1. There is no boundary layer in the zero-buoyancy model (Section 2.2), so we take the MSE of the sub-cloud layer to be that of the lowest atmospheric layer in the simulation. Then, we take the MSE of the cloud layer to be the MSE minimum in the zero-buoyancy model. The theoretical Δh slightly underestimates the simulated values, which increase from 29 kJ/kg to 107 kJ/kg over the experimental range of surface temperatures (Figure 4c). The steady growth in Δh reflects a competition between the increasing latent energy difference and the decreasing dry static energy difference. The vertical latent energy difference represented by $\Delta(Lq)$ is dependent on temperature through the Clausius-Clapeyron relation, explaining its positive rise from 50 kJ/kg to 200 kJ/kg (Figure 4c). A larger and more negative vertical difference in dry static energy of -21 kJ/kg to -92 kJ/kg develops because of the expansion of the troposphere with surface warming. This expansion yields a larger geopotential energy difference in which $\Delta(gz) < 0$, and this cancels out the positive growth in $\Delta(c_p T) > 0$ (not shown). Overall, the growth in Δh is fueled by latent component (Figure 4c).

The equilibrium condition implies that there should be a breakdown of steady, QE convection if CAPE $< \eta \Delta h$. In the simulations of Seeley & Wordsworth (2021a), we see that CAPE$< \eta \Delta h$ above a surface temperature of 320 K (circles in Figure 4a), which coincides with the transition into the RO regime. The zero-buoyancy heat engine model

(lines in Figure 4a) predicts the breakdown of QE convection within 5 K of the onset of RO convection, using QE values of the convective parameters from the simulation (Figure 8b-d). Their simulations show an increase in $\eta\Delta h$ with surface warming largely due to the increase in $\Delta(Lq)$. Convection transports more energy per unit mass of cloudy air in warmer climates. The efficiency of the convective heat engine also increases in warmer climates partly due to the increase in surface temperature and partly due to the radiative properties of water vapor, which shift the emission level upward. In summary, the convection-resolving simulations seem to support our zero-buoyancy heat engine hypothesis: RO convection emerges due to a breakdown in QE convection, which is caused by radiative and thermodynamic effects of increases in water vapor.

4. RO STATES EXIST IN A SINGLE-COLUMN MODEL OF RADIATIVE-CONVECTIVE EQUILIBRIUM

We've demonstrated an important contradiction between quasi-equilibrium convection and radiative-convective equilibrium at high surface temperatures. This led us to a novel explanation for RO emergence. The heat engine (Section 2.1) and zero-buoyancy (Section 2.2) theories of convection posit only the existence of an ensemble of convective plumes that are in steady-state. The heat engine theory acknowledges the potential existence of spatial inhomogeneities in, for instance, radiation, but either averages over them or makes simplifying assumptions to arrive at the useful bulk quantities. In the zero-buoyancy theory, the properties of the environment (this being the sub-saturated downdrafts) including temperature and relative humidity are determined by their mutual interaction with the cloudy updrafts. While this conceptual model is based on three-dimensional reality (Figure 2), the assumption of horizontal homogeneity in temperature of the zero-buoyancy model allows for the governing equations to be evaluated as a function of height alone. Indeed, the only consideration of horizontal variations is implicit in the humidity difference between ascending and descending plumes. These plumes are not spatially resolved but instead their bulk properties are diagnosed from the large-scale environmental variables. Hydrostatic climate models parameterize convective processes in a single vertical dimension using this bulk-plume approach.

We see no a-priori reason why a single-column model of radiative-convective equilibrium should not exhibit RO dynamics at high surface temperatures so long as the convection scheme represents steady-state ascending and descending motion by such a bulk-plume parameterization. As in the case with resolved convection, we should expect RO dynamics in a single-column model of radiative-convective equilibrium if CAPE $< \eta\Delta h$. To test these ideas, we reproduce the basic experimental setup of Seeley & Wordsworth (2021a) in a single-column climate model with a bulk-plume parameterization of convection.

4.1. Model and Methods

We use a version of the ECHAM6 general circulation model (Stevens et al. 2013) in single-column mode that has been modified to allow water vapor to comprise a significant fraction of the atmospheric mass (Popp et al. 2015). The single-column model is forced only by surface heating and radiative cooling (i.e., radiative-convective equilibrium) and has separate schemes for radiation, convection, clouds, and turbulent fluxes.

4.1.1. Base experiment

In our base experiment, we run simulations over a temperature range from 290 K to 360 K. The insolation is set 10% higher than the present-day value and is temporally fixed (no diurnal or seasonal cycle). We set the column latitude to 38°N, where the globally-averaged insolation is the same as the local value. Clouds are the only source of time-varying planetary albedo. The atmosphere is composed *only* of nitrogen, oxygen, carbon dioxide, and water. The molar mixing ratio of carbon dioxide is set to 354 ppmv and is uniform with height. We use a time step of 60 seconds and run the simulations for approximately 200 years. The surface temperature of a 1 m mixed-layer ocean with an albedo of 0.07 is fixed at every time step through the use of an artificial surface heat sink.

4.1.2. Thermodynamics

The version of ECHAM6 that we use accounts for the contribution of water vapor to the total pressure, density, and heat capacity of the atmosphere. The model uses an empirical formula for the saturation vapor pressure of water over liquid and ice, respectively:

$$e^*(\text{Pa}) = \exp\left(c_1/T + c_2 + 10^{-2}c_3T + 10^{-5}c_4T^2 + c_5\ln(T)\right) \tag{57}$$

$$\text{where } c_1, c_2, c_3, c_4, c_5 = \begin{cases} -6024.5282, 29.32707, 1.0613868, -1.3198825, -0.49382577 & \text{if } T \leq 273.15\,\text{K} \\ -6096.9385, 21.2409642, -2.711193, 1.673952, 2.433502 & \text{if } T > 273.15\,\text{K} \end{cases}$$

The constants take different values depending on whether the temperature (in units of Kelvin) is above or below the triple point temperature.

4.1.3. *Radiation*

Shortwave and longwave radiation is resolved into 14 and 16 spectral bands by the Rapid Radiative Transfer Model for General Circulation Models (RRTMG - Iacono et al. 2008). RRTMG uses the correlated-k method under the two-stream approximation, where each band is further sub-divided on the basis of the strength of molecular absorption features. This results in a spectrally-integrated radiative heating rate with 140 pseudo-wavelengths in the longwave and 112 pseudo-wavelengths in the shortwave (Giorgetta et al. 2013). By default, the radiation calculation is performed once hourly. All forms of water besides precipitation are accounted for in the radiation calculation. As in Popp et al. (2015), we use an exponential extrapolation of all molecular absorption coefficients in the longwave and the water self-broadened absorption coefficients in the shortwave for temperatures above which no data in the original model exists. The effect of pressure broadening by water vapor is neglected.

4.1.4. *Convection*

Convection is represented by the Nordeng (1994) bulk-plume scheme, which parameterizes turbulent entrainment and detrainment of air between updrafts, downdrafts, and the environment. The scheme distributes energy, moisture, and momentum through the column under the assumption that the cumulus ensemble is in steady-state. Downdrafts are initialized at the level of free sinking with the properties of a mixture of cloudy and saturated environmental air at their wet bulb temperature (Giorgetta et al. 2013). The level of free sinking is defined as the highest location where said mixture is negatively buoyant with respect to the environment. The downdrafts remain saturated by re-evaporating condensates produced by the convective updrafts. The initial downdraft mass flux is assumed to be directly proportional to the initial updraft mass flux (Nordeng 1994). Note that the zero-buoyancy model of Romps (2016) neglects condensate loading of updrafts (liquid water is instantly removed) and the effect of downdrafts associated with re-evaporation; it does, however, account for adiabatic subsidence in the environment (Section 2.2). For saturated updrafts undergoing pseudo-adiabatic ascent, the bulk-plume equations of Nordeng (1994) are the same as in the zero-buoyancy model of convection (Equations 31 and 33). The convection scheme has a QE-type closure (Neelin & Zeng 2000) so that the cloud-base mass flux $M_{cb} \propto$ CAPE$/\tau$ where $\tau = 2$ hours is an assumed adjustment time for CAPE (Giorgetta et al. 2013).[9] To ensure numerical stability, the permitted range of cloud base mass fluxes is 10^{-10}–1 kg m^{-2}s^{-1} and convective temperature tendencies are limited to 0.05 K/s. We set the entrainment rate in the convection scheme to 0.1 km^{-1}, following Popp et al. (2015) and Spaulding-Astudillo & Mitchell (2023). The updraft mass flux is assumed to be constant up to a critical height set by the buoyancy of entraining convection, above which updrafts are only permitted to detrain (Möbis & Stevens 2012). The downdraft mass flux is assumed to be constant with height (Nordeng 1994; Tiedtke 1989). The trigger for shallow convection is based on the buoyancy of adiabatically lifted parcels relative to the environment at the cloud base (Möbis & Stevens 2012).

As stated above, the single-column model utilizes a QE-type convection scheme. In the context of a convection scheme, "QE" has a specific meaning. Convection schemes require a closure, which is an assumption that enables a prediction of the *instantaneous* convective mass flux. These schemes conceptualize convection as a rapid relaxation process that destroys CAPE. Hence, QE is applied as a concept of balance to the CAPE budget (i.e., the time rate of change of CAPE; Yano & Plant 2012), which describes the time rate of change of CAPE due to radiative and convective processes; the former generates CAPE, while the latter dissipates it. In doing so, the rates of CAPE generation and destruction are assumed to be equal. As discussed, the solution for the instantaneous mass flux in the QE convection scheme is proportional to CAPE (Giorgetta et al. 2013). Notably, however, the *steady-state* heat engine mass flux (Equation 21) is inversely proportional to CAPE. Albeit a technical detail, it is surprising that applying QE reasoning to the entropy budget and the CAPE budget results in formulations of the convective mass flux that seem at odds.

4.1.5. *Clouds*

The large-scale cloud scheme has separate prognostic equations for the vapor, liquid, and ice phases of water, a modified microphysics scheme based on Lohmann & Roeckner (1996), and diagnostic cloud cover (Sundqvist et al. 1989). Sources and sinks of water from non-local transport processes such as convection and turbulence and local

---

[9] This closure to the cloud-base mass flux could conceivably produce large values of M_{cb} if, by some form of convective inhibition, significant CAPE is allowed to build up over a period of time before being released.
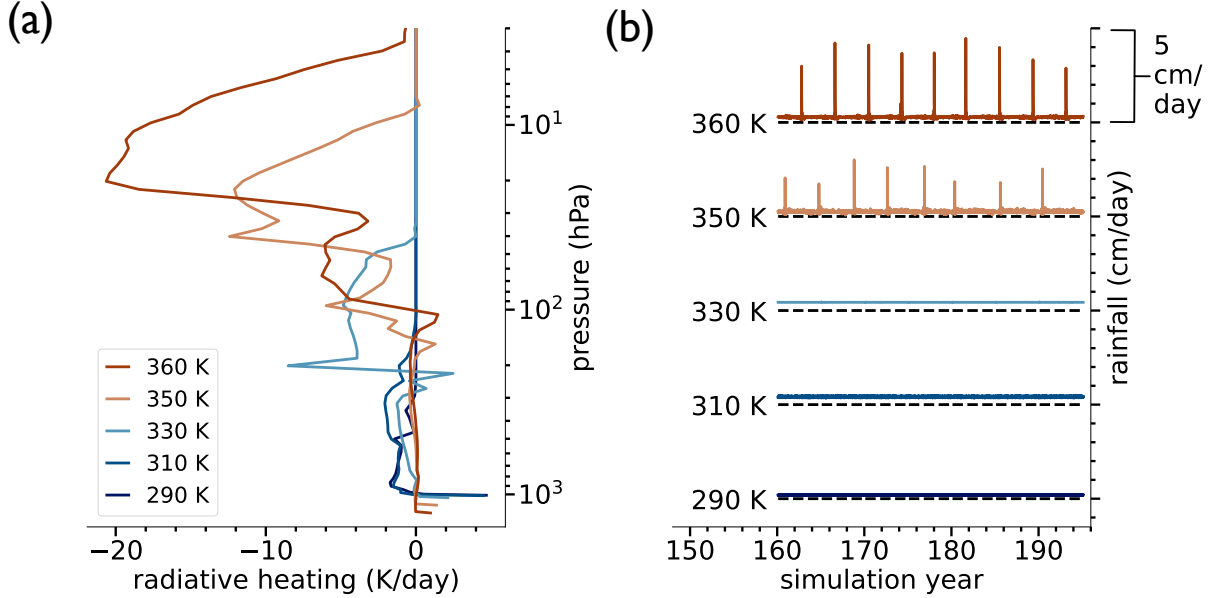
Figure 5. From the base experiment in ECHAM6, (a) net radiative temperature tendency (K/day) and (b) time series of the surface precipitation rate (cm/day). Values in (a) are temporally-averaged over the multi-decadal period in (b). Time is given in years since the start of the simulation. Precipitation rates at each surface temperature are vertically offset by 5 cm/day and a zero rainfall contour is given for reference as a dashed black line.

processes such as condensation, evaporation, deposition, sublimation, precipitation formation, re-evaporation of rain and sublimation of snow are included in the prognostic equations (Giorgetta et al. 2013). The amount of rain re-evaporation at each height is proportional to the local saturation deficit - that is, the difference between the saturation and environmental water vapor mixing ratio (Lohmann & Roeckner 1996). Cloud fraction is diagnosed at each time step as a function of the environmental relative humidity (Stevens et al. 2013). The cloud fraction is calculated only if the relative humidity is greater than a threshold value, which monotonically decreases with height. Condensational growth or evaporative decay of cloud droplets is conditional on whether the relative humidity is above or below this threshold (Giorgetta et al. 2013).

4.1.6. *Surface fluxes and eddy diffusion*

Sensible and latent heat fluxes at the surface are determined by the standard bulk-exchange formulas. Vertical turbulent mixing is parameterized using the eddy-diffusivity approach of Brinkop & Roeckner (1995).

4.1.7. *Precipitation efficiency*

We diagnose the precipitation efficiency in ECHAM6 in accordance with Equation 55, where

$$P_s = P_s^{ls} + P_s^u$$

and

$$SI = SI^{ls} + SI^u.$$

The superscripts "ls" and "u" refer to the large-scale environment and convective updrafts, respectively. P_s^{ls} and P_s^u are surface precipitation rates, which are determined separately by the large-scale cloud scheme and the convection scheme.[10] SI^{ls} and SI^u are the vertically-integrated gross sinks of water vapor associated with phase changes in the large-scale environment and in convective updrafts, respectively. The vertically-integrated gross sink of water vapor in the large-scale environment from the surface (SFC) to the tropopause (TRP) is

$$SI^{ls} = \int_{SFC}^{TRP} \left(\frac{\partial q}{\partial t}\right)^{ls} \frac{dp}{g},$$

---

[10] In a convection-resolving model, there is no distinction between P_s^{ls} and P_s^u.

18

where the gross large-scale sink of water vapor is

$$\left(\frac{\partial q}{\partial t}\right)^{ls} = \dot{q}_{cnd} + \dot{q}_{dep} + \dot{q}_{tbl} + \dot{q}_{tbi} < 0.$$

Here, $\dot{q}_{cnd}$ and $\dot{q}_{dep}$ are the condensation and deposition rates of water vapor, and $\dot{q}_{tbl}$ and $\dot{q}_{tbi}$ are the rates of cloud condensate generation (liquid and ice, respectively) through turbulent fluctuations (Giorgetta et al. 2013). The vertically-integrated sink of water vapor in convective updrafts from the cloud base (CB) to the cloud top (CT)

$$\mathrm{SI}^u = -\int_{\mathrm{CB}}^{\mathrm{CT}} M_u \frac{\partial q_u}{\partial z}\, dz,$$

where M_u is the updraft mass flux and $\frac{\partial q_u}{\partial z} < 0$ is the gross vertical change in updraft specific humidity due to condensation and/or deposition. This definition of SI^u excludes other processes that alter q_u with height but that are not associated with phase changes, such as entrainment. Downdrafts do not generate condensates in ECHAM6; the parameterized effect of downdrafts is to evaporate the condensates produced in updrafts in order to maintain their saturated descent, thereby reducing the overall convective precipitation.

4.2. *RO emergence is consistent with a breakdown of QE*

To date, RO states have only been simulated in Earth models with resolved convection (Seeley & Wordsworth 2021a; Dagan et al. 2023; Song et al. 2024). Figure 5b clearly shows that the simulated climate in our base experiment transitions into the RO state at surface temperatures around 350 K. At cooler temperatures, precipitation is steady with a mean value of 2-6 mm/day; these simulations are in the QE regime. RO states exhibit episodic precipitation with intensities up to 5 cm/day that repeat every $O(100-1000)$ days and that are relatively short-lived (10-30 days).[11] Here, we stress that the storm duration and frequency are inconsistent with previous estimates for hothouse climates. Convection-resolving models find that the storms last several hours and reappear in a matter of days (Seeley & Wordsworth 2021a; Dagan et al. 2023; Song et al. 2024). We speculate that these orders-of-magnitude differences arise from the parameterizations in our one-dimensional model. We cannot rule out the possibility that the driving physics of the RO regime are different between one-dimensional and three-dimensional models. Our partial replication of the RO regime in a single-column model underscores the important limitations of simpler parameterized climate models. The accuracy of the single-column model might be improved by tuning or overhauling existing parameterizations (see Appendix B), a task that we leave to future work.

Nonetheless, the existence of episodic precipitation in our one-dimensional simulations at high surface temperatures allows for a second test of the zero-buoyancy heat engine theory of convection. We determine the range of the convective parameters in the one-dimensional simulations over all surface temperatures to be $0.4 \leq \mathrm{PE} \leq 0.8$ (Figure 8f), $0.55 \leq \mathrm{RH} \leq 0.95$ (Figure 8g), and $0.3 \leq a \leq 7.9$ (Figure 8h). As in Section 3, we use PE and RH from the simulated QE states to diagnose an appropriate value for the bulk-plume parameter a in the single-column model, yielding $\mathrm{PE} = 0.62$, $\mathrm{RH} = 0.81$, and $a = 2.33$ (Figure 8f-h).

CAPE, η, and Δh from the simulations are shown as multi-decadal averages in Figure 6, alongside their predicted values from the theory (η is exempt; see Section 3). The heat transport by convection as measured by the vertical MSE difference increases from 9 kJ/kg to 860 kJ/kg between 290 K and 360 K. The work done by convection as quantified by CAPE ranges from 17 J/kg at 290 K to 194 kJ/kg at 360 K (Figure 6a). The heat engine efficiency increases from $\eta = 12\%$ to 42% over the experimental surface temperature range (Figure 6b). The zero-buoyancy model tends to capture the overall trend of CAPE and Δh in the simulations, though CAPE tends to be over-estimated and under-estimated at low and high surface temperatures, respectively. The theoretical fit to the simulated CAPE can be improved by relaxing the assumption of a single value for PE and a (not shown).

A comparative analysis of the metrics in the equilibrium condition yields several noteworthy findings. The first is that, while the theory reveals a peak in CAPE at intermediate surface temperatures (Seeley & Wordsworth 2023), we observe no clear peak in CAPE in the simulations because the environmental temperatures do not converge on the moist adiabat at high T_s (Figure 6d); this can be understood as the result of the model having a large value of $a \sim 6$ (Figure 8h). The second finding is that quasi-equilibrium is violated (CAPE $< \eta \Delta h$) at intermediate surface

---

[11] The storm duration is calculated as the number of contiguous days where the precipitation rate is above the mean value.

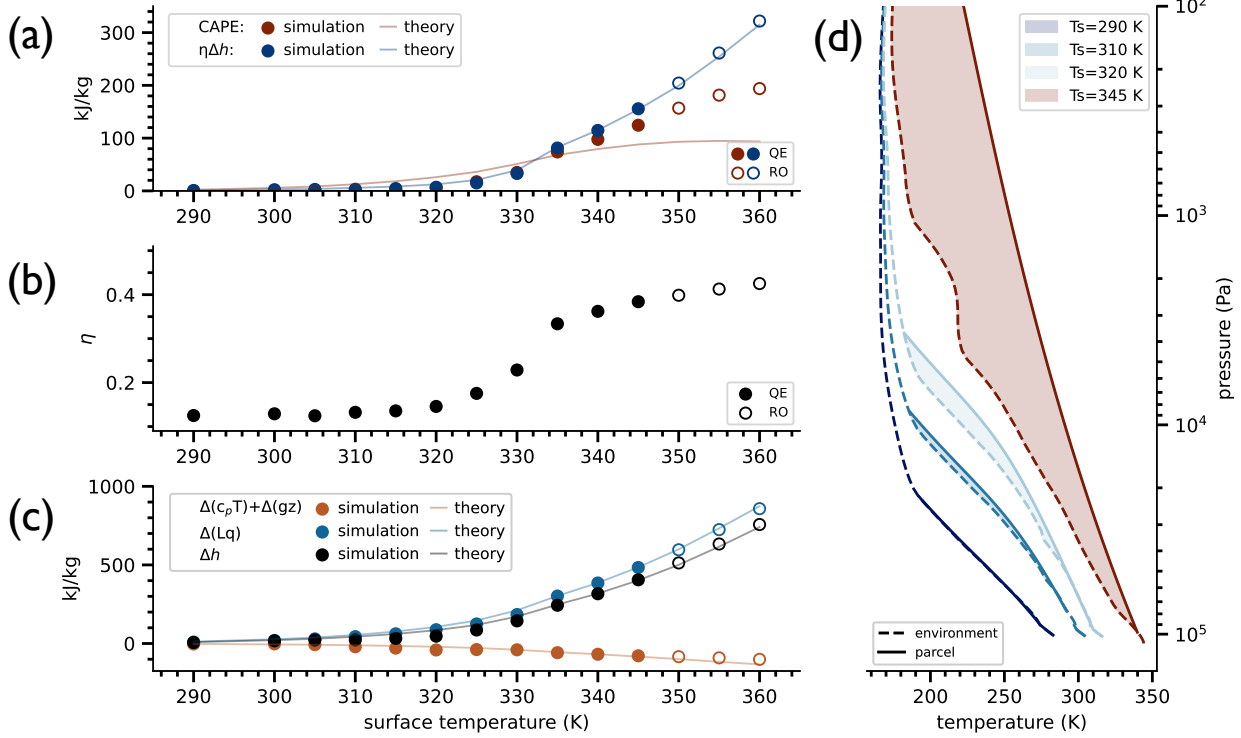ECHAM6 single-column model simulations

Figure 6. (a) Comparison of convective available potential energy (CAPE; Jkg^{-1}) and the vertical moist static energy difference (Δh; Jkg^{-1}) times the heat engine efficiency η as a function of surface temperature. (b) Heat engine efficiency η as a function of surface temperature. (c) Dry $\Delta(c_p T)$ and moist $\Delta(Lq)$ contribution to the moist static energy difference of upward and downward plumes across the LCL as a function of surface temperature. (d) Temperature difference of the environment and an adiabatically-lifted surface parcel in the simulation, given as a proxy for the steady-state CAPE. In (a)-(c), circular markers are diagnosed values from the base experiment with ECHAM6.

temperatures in both the theory and the simulations (approximately 335 K in both cases; Figure 6a). This behavior arises due to the dependence of CAPE, Δh, and η on atmospheric moisture concentration. Specifically, the growth rate of CAPE, unlike Δh, no longer conforms to the Clausius-Clapeyron rate at intermediate surface temperatures (Romps 2016; Seeley & Wordsworth 2023). CAPE is curtailed by its dependence on the tropospheric heat capacity, which is itself affected by the ballooning concentration of water vapor (Seeley & Romps 2015, 2016; Romps 2016). Meanwhile, η increases with surface warming (Figure 6b). Below 320 K, this increase is primarily due to warming the "hot" part of the system. Above 320 K, the radiative effects of water vapor cool the "cold" part of system (i.e., T_a decreases as the net radiating level ascends; Figures 5a and 8e), which raises the efficiency as well. Third, RO-type precipitation is first observed in our simulations at 350 K (Figure 5b). At this surface temperature, quasi-equilibrium is clearly violated (Figure 6a). However, the emergence temperature is 15 K higher than would be predicted under the strictest theoretical interpretation of QE breakdown.[12] Despite the caveats, the one-dimensional simulations seem to support the idea that violating the equilibrium condition (Equation 53) leads to the emergence of RO convection.

5. DISCUSSION

There have been several past studies of hothouse climates on Earth with one-dimensional and three-dimensional models with parameterized convection (Wordsworth & Pierrehumbert 2013; Wolf & Toon 2015; Popp et al. 2015, 2016). All of these studies found low-level temperature inversions in hothouse climates despite different model assumptions,

---

[12] The online ECHAM6 calculation for CAPE uses buoyancy and lapse rate formulations that are behind the state-of-the-art (e.g., Appendix C), which could also influence our offline interpretation of the single-column model results.

however none of them reported episodic precipitation. The models of Wolf & Toon (2015) and Popp et al. (2015, 2016) employ different parameterizations, but the common elements included prognostic water ice, liquid, and vapor (Rasch & Kristjánsson 1998; Lohmann & Roeckner 1996), a bulk-plume convection scheme with quasi-equilibrium closure (Zhang & McFarlane 1995; Nordeng 1994), two-stream radiative transfer using the correlated-k method (Wolf & Toon 2013; Iacono et al. 2008), parameterized ocean heat transport, and prognostic surface temperatures. In the three-dimensional studies, Wolf & Toon (2015) included a seasonal cycle with modern ocean-land surface configuration, whereas Popp et al. (2016) simulated a global aquaplanet with no seasonal cycle. Seeley & Wordsworth (2021a) were the first to report episodic precipitation in hothouse climates using a (regional) cloud-resolving model. For our single-column model simulations, we employed the same model as Popp et al. (2015, 2016) in single-column mode with parameterized convection, but we followed the experimental setup of Seeley & Wordsworth (2021a) with 10% higher insolation than present-day, a mixed-layer ocean, and fixed sea surface temperatures. Under these experimental conditions, the single-column model produces episodic precipitation at high surface temperatures.

It seems clear that relaxation-oscillator (RO) convection emerges in sufficiently warm and/or humid atmospheres. A novelty of this work is that RO convection is not only possible in convection-resolving, three-dimensional simulations (Seeley & Wordsworth 2021a; Dagan et al. 2023), but also in a single-column climate model with parameterized convection. That being said, the RO-type convection and precipitation that develops in our single-column simulations does not closely resemble the characteristics of RO convection in three-dimensional convection-resolving simulations (Seeley & Wordsworth 2021a), which we address below.

A second novelty of this work is the development of an even simpler model for the emergence of RO convection; we hypothesized that RO convection emerges in warm/humid climates due to a breakdown of QE convection, and developed a predictive theory based on a heat engine model for convection. In QE, the rate of atmospheric radiative cooling can be related to a rate of work (Equation 20), which is proportional to the mass flux and CAPE. In sufficiently warm and humid atmospheres, the steady-state storage of CAPE is curtailed (Seeley & Wordsworth 2023) as heating goes to the latent reservoir instead of increasing temperature and buoyancy (Romps 2016). The change in CAPE with surface warming can be calculated using an analytical theory of convection in which entraining plumes are neutrally buoyant with respect to their environment (Romps 2016), as cloudy regions are observed to be in Earth's tropics (Singh & O'Gorman 2013). Holding radiative cooling fixed, QE demands that the convective mass flux *increase* with decreasing CAPE (Equation 21), as must occur at high temperatures where CAPE is decreasing. However, because the mass and energy budget of the convection must close in the sub-cloud layer, radiative cooling aloft is counterbalanced by convective heat transport, i.e. the MSE flux across the LCL. It's intuitive that the MSE flux can grow rapidly as the surface temperature increases due to the exponential increase in saturation vapor pressure. Again holding radiative cooling fixed, this implies the sub-cloud mass flux must *decrease* with increasing surface temperatures (Equation 25). If the sub-cloud layer cannot supply the cloud layer with enough mass flux, there can be no QE state – an inevitable consequence of the growing disparity between the increase in energy of the sub-cloud layer and a slower increase and/or decrease in CAPE. This follows from the equilibrium condition (Equation 53) of a convective heat engine, which requires (i) a statistical equivalence between vertical heat transport ($|M_{sc}| \times \Delta h$; Equation 25) and radiative cooling (F_a; Equation 6) and (ii) the conversion of surface heating into work ($|M| \times$ CAPE; Equation 20) at a thermodynamic efficiency (η; Equation 16).

In addition to our theoretical arguments, we presented evidence from simulations with and without resolved convection in support of the idea that the RO mode of convection is preferred in conditions that violate the equilibrium condition. We emphasize that our analysis does not rule out the lower-tropospheric radiative heating hypothesis of Seeley & Wordsworth (2021a) as an explanation for RO emergence (see below); future work should compare these differing perspectives. Our analysis was first performed on convection-resolving model data from Seeley & Wordsworth (2021a). We found that the equilibrium condition is violated around 320 K, which is consistent with the temperature of RO emergence in their simulations. We repeated the analysis on data from our one-dimensional model and found that $\eta\Delta h$ first exceeds CAPE around 335 K, but that episodic precipitation emerges closer to 350 K. The RO state clearly emerges in conditions that violate QE, but the accuracy of the theoretical prediction is worse when applied to the single-column model. The heat engine perspective of convection suggests that the conditions that make the QE state energetically unsustainable – in this case, curtailed growth in CAPE and sustained increases in atmospheric heat transport and opacity with surface warming – causes the RO state to emerge. It is possible to obtain episodic convection in a one-dimensional climate model because modern parameterizations are able to represent the necessary physics in a single vertical dimension. This possibility is underscored by our usage of the bulk-plume equations of

convection in the zero-buoyancy heat engine theory, which are, in turn, a simplified version of the Nordeng (1994) convection scheme in our one-dimensional climate model (Section 4.1). The existence of the QE-to-RO convective regime transition across the modeling hierarchy[13] explored here lends confidence to the robustness of this transition, and we have demonstrated that important insights can be gained from the simpler end of the modeling hierarchy.

Next, we discuss how our heat engine hypothesis connects with previous work on RO convection, starting with the discovery paper: Seeley & Wordsworth (2021a). They found that the QE-to-RO transition coincides with the critical temperature at which the water vapor window closes, implying that LTRH is crucial for the emergence of RO states. However, subsequent studies by Dagan et al. (2023) and Song et al. (2024) challenged this hypothesis, demonstrating that RO states can occur in the absence of LTRH. Specifically, Dagan et al. (2023) suggested that while LTRH can be sufficient for the emergence of RO states in some cases, it is not a necessary condition. Meanwhile, Song et al. (2024) investigated whether vertical contrasts in radiative cooling are more critical than the sign of the cooling rate in a specific atmospheric layer. They varied the magnitude of imposed cooling profiles in the lower and upper troposphere separately at a fixed surface temperature of 325 K. Their experiments revealed QE-to-RO transitions in response to substantial increases in upper-tropospheric radiative cooling or decreases in lower-tropospheric radiative cooling. In contrast, when radiative cooling was uniformly increased across the entire troposphere, no QE-to-RO transition occurred. These findings align with our theory, which posits that the efficiency η is proportional to the difference between the inverse temperatures at which the engine absorbs ($1/T_s$) and emits ($1/T_a$) energy. Our simulations show that T_a decreases with increasing surface temperature above 320 K, leading to an increase in heat engine efficiency with warming (Figure 6b), and this promotes QE breakdown. Given that T_s is fixed in Song et al. (2024)'s experiments, the emission-weighted atmospheric temperature, T_a, becomes critical.[14] All else equal, adding a constant to the radiative cooling at all levels would exactly cancel out in the weighted average for T_a, which is consistent with the absence of a QE-to-RO transition in these runs in Song et al. (2024). Conversely, all else equal, enhancing upper-level cooling or suppressing lower-level cooling would decrease T_a, potentially leading to a violation of the equilibrium condition if Δh and CAPE remain constant. To maintain quasi-equilibrium, what "matters" more is not the rate at which heat is lost, but rather the temperature at which that heating or cooling occurs. This lesson is qualitatively consistent with the primary findings of Song et al. (2024).

The theory that we've developed tells us when steady convection *must* break down, but not necessarily *how* it happens. This limitation is intrinsic to equilibrium models, where there are no net forces. While it is reasonable to infer that steady convection ceases where quasi-equilibrium is incompatible with radiative-convective equilibrium, these constraints do not give insight into the physical forces acting on convective plumes at the QE-to-RO transition. Consequently, a common approach for determining why RO convection happens is to look for changes in CIN (Equation 2). In the non-equilibrium perspective, the presence of stable layers inhibits convection and delays convective triggering. There are several studies that have considered the effects of water vapor on inhibition (Li & Ingersoll 2015; Seeley & Wordsworth 2021a). For example, water vapor plays an important role in modulating convective activity in Saturn's atmosphere. The high molecular weight of water vapor compared to the non-condensing background gases suppresses convection until the slow cooling of the atmosphere makes it unstable. This mechanism has been put forward as an explanation for the intermittent, giant storms on Saturn (Li & Ingersoll 2015). In addition, the LTRH that is induced by water vapor in Earth's hothouse climates is important for generating very stable layers, including near-surface temperature inversions (Wordsworth & Pierrehumbert 2013; Wolf & Toon 2015; Popp et al. 2015). These inversions cap the boundary layer, decoupling it from the overlying atmosphere, and are slowly eroded by re-evaporation processes associated with descending virga. Seeley & Wordsworth (2021a) demonstrated that imposing LTRH can tip the climate into the RO state. We speculate that this is also due to a breakdown of QE because LTRH likely increases η by changing the effective absorbing and emitting temperatures, and reduces CAPE and/or introduces CIN. We leave it to future work to test this.

In our derivation of the zero-buoyancy heat engine model, we made a few notable assumptions, approximations, and omissions that introduce errors in the limit of a moisture-dominated atmosphere. Revisiting these assumptions is a necessary next step, but is beyond the scope of this paper. First, we assumed that a statistical balance exists between sources and sinks of entropy in Earth's climate system (Equation 3), and furthermore that the dominant source is frictional dissipation and that the dominant sink is absorption and emission of radiation. This yields a prediction for

---

[13] Our usage of the term "model hierarchy" differs from the conventional definition, which refers to an tiered system of models with each subsequent tier operating at a higher level of complexity.

[14] The mean temperature at which frictional dissipation occurs, T_d, is also likely to be important.

the temperature of RO emergence, though at the cost of neglecting other potential sources of entropy generation. A simple balance between frictional dissipation and radiation is an excellent approximation in numerical simulations of dry convection (Pauluis & Held 2002a), and is also somewhat reasonable for moist convection on Earth. Irreversible mixing, phase changes, and hydrometeor drag are likely the dominant sources of entropy generation in Earth's current atmosphere (Pauluis & Held 2002a,b; Romps 2008; Singh & O'Neill 2022). Frictional dissipation (which includes hydrometeor drag) accounts for almost half of the total entropy generation in convection-resolving simulations (Singh & O'Gorman 2016). To improve our prediction of RO emergence, one could include the omitted processes in the entropy budget ($\Delta\dot{S}$; Equation 14) and repeat our analysis. Second, we neglected the potentially-important role of CIN in the vertical integral of buoyancy (Equation 52) and assumed that updrafts and downdrafts contribute equally to the buoyancy flux. Third, we made an important omission in the zero-buoyancy theory of convection: the virtual effect of the condensable gas. The virtual effect impacts the magnitude of CAPE, particularly in condensable-rich atmospheres. Further exploration of these limitations is left to future work.

Our single-column model fails on important benchmarks set by convection-resolving models (Seeley & Wordsworth 2021a; Dagan et al. 2023). First, the latter models agree that RO states on Earth should have a storm duration of several hours with an intervening period of several days. Our model produces storms with a duration of a few weeks that reoccur every few years. This could be related to the high PE of the single-column model simulations (Figure 8f), which we suspect is related to the non-zero precipitation during calm intervals in Figure 5b; the convection scheme seems to have a minimum threshold for precipitation whether or not it would re-evaporate in lower layers due to a built-in assumption that there is no environmental re-evaporation of condensates above the base of the convective updrafts (see Appendix B). The model also produces very high values of CAPE, which can be understood by the large value of the inferred bulk plume parameter a that prevents the environment from becoming moist adiabatic. Second, our model transitions into the RO state at temperatures above 350 K, which is 30 K higher than in convection-resolving model simulations (Seeley & Wordsworth 2021a; Dagan et al. 2023; Song et al. 2024). This could be due to the large values of CAPE of the single-column model, which again is due to the large value of a; Figure 3a demonstrates that increasing CAPE values drives the QE breakdown to higher temperatures. See Appendix B for more details. The performance of the single-column model depends on the parameterizations and the assumptions made in developing them. These simple models are typically tuned to the modern climate of the planet they are meant to represent, and therefore are not guaranteed to represent reality in extreme scenarios. If the RO states in our single-column model are indeed driven by the same physics as in a convection-resolving model, then it is clear that our model suffers from poor realism, and we suspect the convective parameterization is to blame. It's conceivable that with some additional tuning, the single-column model could improve relative to the cloud-resolving models.

6. IMPLICATIONS FOR TITAN

While present-day Earth does not exhibit RO behavior (Figure 1a), it is clear that episodic storms of potentially great magnitude occur on present-day Titan (Schneider et al. 2012; Turtle et al. 2011b; Faulk et al. 2017; Rafkin et al. 2022; Charnay et al. 2015; Mitchell & Lora 2016). Global simulations of Titan with realistic land surface hydrology by Faulk et al. (2020) with the Titan Atmospheric Model (Lora et al. 2015) depicted in Figure 1b resemble the one-dimensional (Figure 5d) and three-dimensional (Figure 1c; Seeley & Wordsworth 2021a) simulated RO states on Earth, where brief periods of intense rainfall give way to extended periods of little to no rain. The intermittent cloud formation (and precipitation by inference) on Titan is presently understood to result from a combination of large-scale and convective-scale dynamics (Mitchell et al. 2006). Titan's cloud-forming regions undergo seasonal migration and concentrate near the summer pole due to thermally-direct global circulation promoting ascent in this area (Turtle et al. 2011a; Mitchell & Lora 2016). However, cloud formation is also driven by local convection related to seasonal changes in temperature and near-surface moisture (Brown et al. 2002). Observations support this, showing that high-latitude clouds often form in convectively unstable layers (Griffith et al. 2000; Hörst 2017). Given sufficient convective instability, storms can be triggered by poleward-propagating Rossby waves (Battalio & Lora 2021). A regional convective outburst can also have a global impact (Battalio & Lora 2021; Turtle et al. 2011a) through Rossby wave generation leading to outbreaks in other regions, such as over Titan's low-latitude deserts (Schaller et al. 2009; Turtle et al. 2011b).

The observed interval between large cloud systems on Titan is approximately 3-18 months (Roe 2012), which might indicate the frequency of surface precipitation. To reproduce the frequency of these cloud-forming events, convective parameterizations in global climate models of Titan have to be tuned (Battalio et al. 2022). The Titan Atmospheric Model (Lora et al. 2015), from which the data in Figure 1b originates, uses a simple Betts-Miller convection scheme
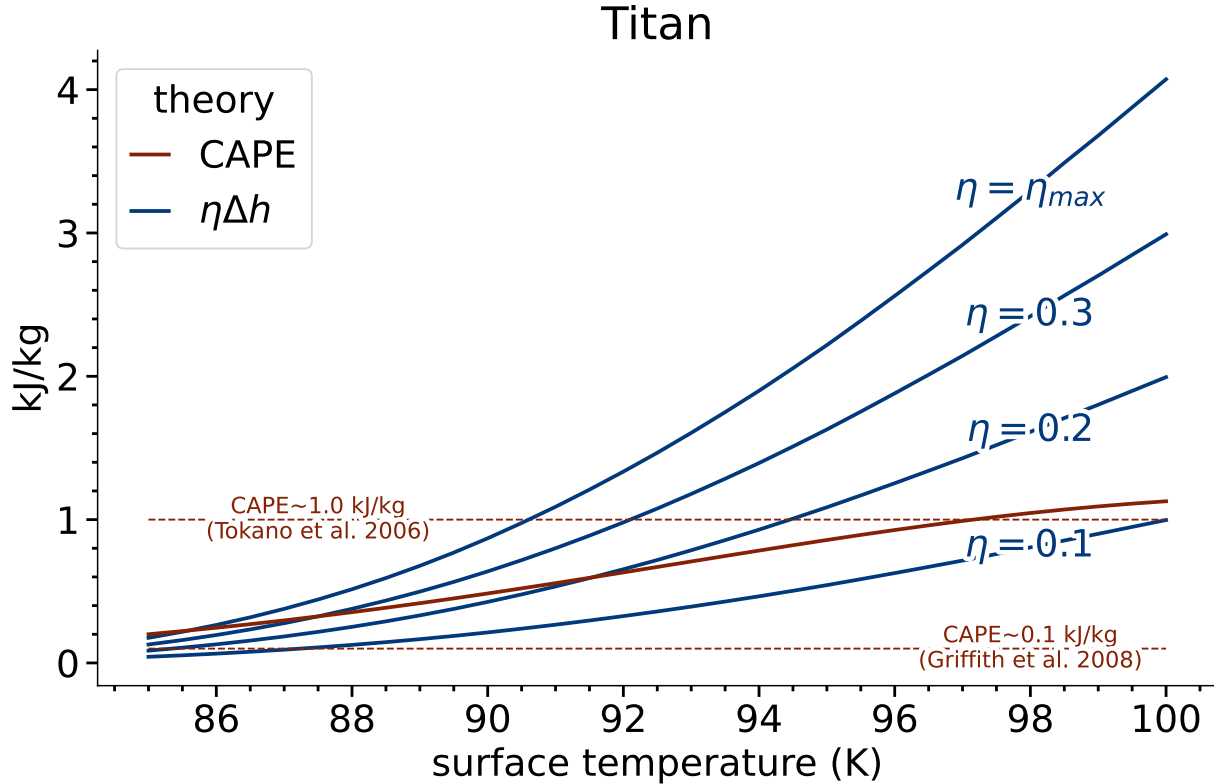
Figure 7. Theoretical CAPE (solid orange) and $\eta\Delta h$ (solid blue) for a Titan-like atmosphere from the zero-buoyancy heat engine model. In addition to the parameter choices for Titan in Appendix A, we set $a = 0.33$ and PE $= 0.2$. Multiple labeled $\eta\Delta h$ curves show a hypothetical range of η values between 0.1 and $\eta_{max} = (T_s - T_{trp})/T_{trp}$. Estimates of CAPE on Titan using the Huygens probe measurements disagree, with the estimates (dashed orange) ranging from $\sim$0.1 kJ/kg (Griffith et al. 2008) to $\sim$1 kJ/kg (Tokano et al. 2006).

801 (Frierson 2007). In this scheme, convection is triggered when CAPE $-$ CIN > 0. Local conditions determine whether
802 the triggered convection is precipitating or not. If the relative humidity is less (greater) than a preset reference value
803 (RH$_{ref}$), then non-precipitating (precipitating) convection occurs. Using the value of RH$_{ref}$ most consistent with the
804 observed frequency of Titan's storms, the best-fit simulations from Battalio et al. (2022) show a global-mean CAPE
805 of 40 J/kg and a global-mean CIN of 50 J/kg. The authors attribute the existence of rare convective storms in their
806 model to the fact that CAPE $-$ CIN < 0. In comparison, Earth's global-mean CAPE is 300 J/kg and global-mean
807 CIN is 20 J/kg (Riemann-Campe et al. 2009). On the basis of the parameterization design, we would expect the same
808 convection scheme in an Earth climate model to produce continuous precipitation. In the Titan study (Battalio et al.
809 2022), for example, the authors report a fundamental shift from episodic to continuous precipitation that occurs when
810 CAPE $-$ CIN changes sign, consistent with this interpretation. Though some insight into the nature of Titan's episodic
811 precipitation can be gained from the parameterizations in GCMs, regional or global convection-resolving simulations
812 of Titan are needed.
813 The alignment of the climate of Titan and the hothouse Earth also merits further study. One example of this
814 alignment is their total precipitable moisture: that is, the depth of liquid that would one would obtain by condensing
815 out all atmospheric moisture into a uniform layer at the surface. Titan's atmosphere stores around 5 m of precipitable
816 methane (Tokano et al. 2006). Though the globally-averaged surface temperature on Earth is nearly 200 K warmer,
817 the total precipitable moisture in Earth's atmosphere - just a few centimeters of water - is smaller because water on
818 Earth has a volatility[15] ten times less than methane on Titan (Griffith et al. 2008; Spaulding-Astudillo & Mitchell

---

[15] Volatility is here defined as the saturation vapor pressure of a condensable at the typical temperature of the planetary surface.

2023). A consequence of the high temperatures in the hothouse climate is that the total precipitable water rises above 0.5 m by 330 K (Seeley & Wordsworth 2021b), or to within an order of magnitude of the precipitable methane in Titan's atmosphere. Since the latent heat of condensation of water is about an order of magnitude larger than that for methane (Appendix A), the latent energy reservoir (expressed in per unit area) in the hothouse climate is remarkably similar to Titan, which has important implications for moist convection.

Titan represents a unique laboratory for further testing of the zero-buoyancy heat engine theory of convection. To illustrate this, we carry out a back-of-the-envelope calculation of the equilibrium condition for Titan (Figure 7) with the parameter values in Appendix A. The only direct measurement of CAPE in Titan's atmosphere comes from the Huygens probe, which landed at 10°S where the near-surface relative humidity was $\sim 50\%$ (Mitchell & Lora 2016). Estimates of CAPE at the time and location of the Huygen's probe descent vary, with values of 960 J/kg (Tokano et al. 2006), 60 J/kg (Barth & Rafkin 2007), and 120 J/kg (Griffith et al. 2008) reported. The disparity in these values supposedly stems from different formulations of the adiabatic lapse rate (Griffith et al. 2008). To the best of our knowledge, no direct estimation of the MSE profile at the Huygens landing site exists. Therefore, we rely on the spatially- and temporally-averaged vertical MSE difference from Titan Atmospheric Model simulations (Figure 1b; Faulk et al. 2020), yielding $\Delta h \approx 2500$ J/kg. MSE is well-mixed in the boundary layer and decreases with height from 5 km to 15 km, where the MSE minimum occurs (not shown). Since the surface temperature at Titan's equator is $\sim$95 K and the equator-to-pole temperature gradient is weak (only 2-4 K; Jennings et al. 2011), a typical surface temperature on Titan is likely 92 K. Configured to Titan-like conditions, the zero-buoyancy model predicts that CAPE$\sim$600 J/kg and $\Delta h \sim$3300 J/kg at 92 K (Figure 7). Theoretically, QE breakdown could occur on Titan if $\eta \geq 20\%$ at 92 K. However, a realistic estimate of η on Titan is still needed for comparison with the zero-buoyancy heat engine model. Obtaining this would require convection-resolving simulations with realistic radiation, as η depends on the unique radiative properties of Titan's atmosphere. On Earth, water vapor is the dominant greenhouse gas and sets the mean tropospheric cooling rate (Held & Soden 2000; Jeevanjee & Fueglistaler 2020). Radiative processes are more complex on Titan, where the major source of infrared opacity is from collision-induced absorption of nitrogen, methane, and hydrogen (McKay et al. 1991). Titan's atmosphere is also strongly absorbing at solar wavelengths; 80% of the incident flux is absorbed by the atmosphere and 10% at the surface (Tomasko et al. 2008).

An interesting question for future work is whether the dynamical similarity of Titan and the hothouse Earth can be linked to the breakdown of QE convection in both cases. The conceptual framework that we've proposed offers a robust point of comparison between planetary atmospheres based on the first and second laws of thermodynamics, which are system invariant. The theory is, moreover, agnostic of the composition of the working fluid and thus seems a promising framework to explore the dynamical similarity between Titan and the hothouse Earth. The theory could be extended to any planetary atmosphere with a condensing component and, because of this, it will find wide application in the solar system and beyond.

OPEN RESEARCH

The data from this study (Spaulding-Astudillo & Mitchell 2024) is available at https://doi.org/10.5281/zenodo.10982231.

REFERENCES

Arakawa, A., & Schubert, W. H. 1974, Journal of Atmospheric Sciences, 31, 674 , doi: https://doi.org/10.1175/1520-0469(1974)031⟨0674: IOACCE⟩2.0.CO;2

Barth, E. L., & Rafkin, S. C. R. 2007, Geophysical Research Letters, 34, doi: https://doi.org/10.1029/2006GL028652

Battalio, J. M., & Lora, J. M. 2021, Geophysical Research Letters, 48, e2021GL094244, doi: https://doi.org/10.1029/2021GL094244

Battalio, J. M., Lora, J. M., Rafkin, S., & Soto, A. 2022, Icarus, 373, 114623, doi: 10.1016/j.icarus.2021.114623

Bjerknes, J. 1938, Q.J.R. Meteorol. Soc., 64, 325

Brinkop, S., & Roeckner, E. 1995, Tellus A, 47, 197, doi: https://doi.org/10.1034/j.1600-0870.1995.t01-1-00004.x

Brown, M. E., Bouchez, A. H., & Griffith, C. A. 2002, Nature, 420, 795, doi: 10.1038/nature01302

Charnay, B., Barth, E., Rafkin, S., et al. 2015, Nature Geoscience, 8, 362, doi: 10.1038/ngeo2406

Chen, D., Dai, A., & Hall, A. 2021, Journal of Geophysical Research: Atmospheres, 126, e2020JD034198, doi: https://doi.org/10.1029/2020JD034198

Dagan, G., Seeley, J. T., & Steiger, N. 2023, Journal of Advances in Modeling Earth Systems, 15, e2023MS003765, doi: https://doi.org/10.1029/2023MS003765

Dhingra, R. D., Barnes, J. W., Brown, R. H., et al. 2019, Geophysical Research Letters, 46, 1205, doi: https://doi.org/10.1029/2018GL080943

Emanuel, K. 2001, International Geophysics, 70, 225, doi: 10.1016/S0074-6142(00)80056-X

Emanuel, K. A. 1986, Journal of Atmospheric Sciences, 43, 585 , doi: https://doi.org/10.1175/1520-0469(1986)043⟨0585: AASITF⟩2.0.CO;2

—. 1994, Atmospheric convection / Kerry A. Emanuel. (New York: Oxford University Press)

Emanuel, K. A., & Bister, M. 1996, Journal of Atmospheric Sciences, 53, 3276 , doi: https://doi.org/10.1175/1520-0469(1996)053⟨3276: MCVABS⟩2.0.CO;2

Faulk, S. P., Lora, J. M., Mitchell, J. L., & Milly, P. C. D. 2020, Nature Astronomy, 4, 390, doi: 10.1038/s41550-019-0963-0

Faulk, S. P., Mitchell, J. L., Moon, S., & Lora, J. M. 2017, Nature Geoscience, 10, 827, doi: 10.1038/ngeo3043

Frierson, D. M. W. 2007, Journal of the Atmospheric Sciences, 64, 1959 , doi: 10.1175/JAS3935.1

Gelaro, R., McCarty, W., Suárez, M. J., et al. 2017, Journal of Climate, 30, 5419 , doi: https://doi.org/10.1175/JCLI-D-16-0758.1

Giorgetta, M., Roeckner, E., Mauritsen, T., & Rast, S. 2013, Berichte zur Erdsystemforschung / Max-Planck-Institut für Meteorologie, 135

Griffith, C. A., Hall, J. L., & Geballe, T. R. 2000, Science, 290, 509, doi: 10.1126/science.290.5491.509

Griffith, C. A., McKay, C. P., & Ferri, F. 2008, The Astrophysical Journal, 687, L41, doi: 10.1086/593117

Griffith, C. A., Owen, T., Geballe, T. R., Rayner, J., & Rannou, P. 2003, Science, 300, 628, doi: 10.1126/science.1081897

Griffith, C. A., Owen, T., Miller, G. A., & Geballe, T. 1998, Nature, 395, 575, doi: https://doi.org/10.1038/26920

Held, I. M., & Soden, B. J. 2000, Annual Review of Energy and the Environment, 25, 441, doi: 10.1146/annurev.energy.25.1.441

Hörst, S. M. 2017, Journal of Geophysical Research: Planets, 122, 432, doi: https://doi.org/10.1002/2016JE005240

Iacono, M. J., Delamere, J. S., Mlawer, E. J., et al. 2008, Journal of Geophysical Research: Atmospheres, 113, doi: 10.1029/2008JD009944

Jeevanjee, N., & Fueglistaler, S. 2020, Journal of the Atmospheric Sciences, 77, 465 , doi: https://doi.org/10.1175/JAS-D-18-0352.1

Jennings, D. E., Cottini, V., Nixon, C. A., et al. 2011, The Astrophysical Journal Letters, 737, L15, doi: 10.1088/2041-8205/737/1/L15

Koll, D. D. B., & Cronin, T. W. 2018, Proceedings of the National Academy of Sciences, 115, 10293, doi: 10.1073/pnas.1809868115

Lewis-Merrill, R. A., Moon, S., Mitchell, J. L., & Lora, J. M. 2022, The Planetary Science Journal, 3, 223, doi: 10.3847/PSJ/ac8d09

Li, C., & Ingersoll, A. P. 2015, Nature Geoscience, 8, 398, doi: 10.1038/ngeo2405

Liu, J., Yang, J., Ding, F., Chen, G., & Hu, Y. 2024, Science Advances, 10, eado2515, doi: 10.1126/sciadv.ado2515

Lohmann, U., & Roeckner, E. 1996, Climate Dynamics, 12, 557, doi: 10.1007/BF00207939

Lora, J. M., Lunine, J. I., & Russell, J. L. 2015, Icarus, 250, 516, doi: 10.1016/j.icarus.2014.12.030

Marquet, P. 2016, Journal of the Atmospheric Sciences, 73, 2565 , doi: 10.1175/JAS-D-15-0299.1

McKay, C. P., Pollack, J. B., & Courtin, R. 1991, Science, 253, 1118, doi: 10.1126/science.11538492

Mitchell, J. L., & Lora, J. M. 2016, Annual Review of Earth and Planetary Sciences, 44, 353, doi: 10.1146/annurev-earth-060115-012428

Mitchell, J. L., Pierrehumbert, R. T., Frierson, D. M. W., & Caballero, R. 2006, Proceedings of the National Academy of Sciences, 103, 18421, doi: 10.1073/pnas.0605074103

Möbis, B., & Stevens, B. 2012, Journal of Advances in Modeling Earth Systems, 4, 1, doi: 10.1029/2012MS000199

Neelin, J. D., & Zeng, N. 2000, Journal of the Atmospheric Sciences, 57, 1741 , doi: https://doi.org/10.1175/1520-0469(2000)057⟨1741: AQETCM⟩2.0.CO;2

26

Nordeng, E. T. 1994, Research Department Technical Memorandum, 206, 1

Pauluis, O., & Held, I. M. 2002a, Journal of the Atmospheric Sciences, 59, 125 , doi: https://doi.org/10.1175/1520-0469(2002)059⟨0125: EBOAAI⟩2.0.CO;2

—. 2002b, Journal of the Atmospheric Sciences, 59, 140 , doi: https://doi.org/10.1175/1520-0469(2002)059⟨0140: EBOAAI⟩2.0.CO;2

Perron, J. T., Lamb, M. P., Koven, C. D., et al. 2006, Journal of Geophysical Research: Planets, 111, doi: https://doi.org/10.1029/2005JE002602

Pierrehumbert, R. T. 2010, Principles of Planetary Climate (Cambridge University Press), doi: 10.1017/CBO9780511780783

Popp, M., Schmidt, H., & Marotzke, J. 2015, Journal of the Atmospheric Sciences, 72, 452, doi: 10.1175/JAS-D-13-047.1

—. 2016, Nature Communications, 7, 10627, doi: 10.1038/ncomms10627

Rafkin, S. C., Lora, J. M., Soto, A., & Battalio, J. M. 2022, Icarus, 373, 114755, doi: 10.1016/j.icarus.2021.114755

Rasch, P. J., & Kristjánsson, J. E. 1998, Journal of Climate, 11, 1587 , doi: https://doi.org/10.1175/1520-0442(1998)011⟨1587: ACOTCM⟩2.0.CO;2

Rennó, N. O., & Ingersoll, A. P. 1996, Journal of Atmospheric Sciences, 53, 572 , doi: https://doi.org/10.1175/1520-0469(1996)053⟨0572: NCAAHE⟩2.0.CO;2

Riemann-Campe, K., Fraedrich, K., & Lunkeit, F. 2009, Atmospheric Research, 93, 534, doi: 10.1016/j.atmosres.2008.09.037

Roe, H. G. 2012, Annual Review of Earth and Planetary Sciences, 40, 355, doi: 10.1146/annurev-earth-040809-152548

Romps, D. M. 2008, Journal of the Atmospheric Sciences, 65, 3779 , doi: 10.1175/2008JAS2679.1

—. 2014, Journal of Climate, 27, 7432, doi: 10.1175/JCLI-D-14-00255.1

—. 2015, Journal of the Atmospheric Sciences, 72, 3639 , doi: 10.1175/JAS-D-15-0054.1

—. 2016, Journal of the Atmospheric Sciences, 73, 3719 , doi: 10.1175/JAS-D-15-0327.1

Romps, D. M., Charn, A. B., Holzworth, R. H., et al. 2018, Geophysical Research Letters, 45, 12,623, doi: https://doi.org/10.1029/2018GL080267

Schaller, E. L., Roe, H. G., Schneider, T., & Brown, M. E. 2009, Nature, 460, 873, doi: 10.1038/nature08193

Schneider, T., Graves, S. D. B., Schaller, E. L., & Brown, M. E. 2012, Nature, 481, 58, doi: 10.1038/nature10666

Seeley, J. T., & Romps, D. M. 2015, Geophysical Research Letters, 42, 10,429, doi: https://doi.org/10.1002/2015GL066199

—. 2016, Geophysical Research Letters, 43, 3572, doi: https://doi.org/10.1002/2016GL068583

Seeley, J. T., & Wordsworth, R. D. 2021a, Nature, 599, 74, doi: 10.1038/s41586-021-03919-z

—. 2021b, Data and code for Seeley and Wordsworth (2021), "Episodic deluges in simulated hothouse climates", Zenodo, doi: 10.5281/zenodo.5636455

—. 2023, The Planetary Science Journal, 4, 34, doi: 10.3847/PSJ/acb0cb

Seidel, S. D., & Yang, D. 2020, Science Advances, 6, eaba1951, doi: 10.1126/sciadv.aba1951

Singh, M. S., & O'Gorman, P. A. 2013, Geophysical Research Letters, 40, 4398, doi: 10.1002/grl.50796

—. 2016, Journal of Advances in Modeling Earth Systems, 8, 1132, doi: https://doi.org/10.1002/2016MS000673

Singh, M. S., & O'Neill, M. E. 2022, Rev. Mod. Phys., 94, 015001, doi: 10.1103/RevModPhys.94.015001

Sobel, A. H., Nilsson, J., & Polvani, L. M. 2001, Journal of the Atmospheric Sciences, 58, 3650 , doi: 10.1175/1520-0469(2001)058⟨3650: TWTGAA⟩2.0.CO;2

Song, X., Abbot, D. S., & Yang, J. 2024, Journal of Advances in Modeling Earth Systems, 16, e2023MS003912, doi: https://doi.org/10.1029/2023MS003912

Spaulding-Astudillo, F. E., & Mitchell, J. L. 2023, Journal of the Atmospheric Sciences, doi: 10.1175/JAS-D-22-0063.1

—. 2024, Data for Spaulding-Astudillo and Mitchell (2024a), "A simple model for the emergence of relaxation-oscillator convection", Zenodo, doi: 10.5281/zenodo.10982231

Stevens, B., Giorgetta, M., Esch, M., et al. 2013, Journal of Advances in Modeling Earth Systems, 5, 146, doi: 10.1002/jame.20015

Sui, C.-H., Li, X., & Yang, M.-J. 2007, Journal of the Atmospheric Sciences, 64, 4506 , doi: 10.1175/2007JAS2332.1

Sundqvist, H., Berge, E., & Kristjánsson, J. E. 1989, Monthly Weather Review, 117, 1641, doi: 10.1175/1520-0493(1989)117⟨1641: CACPSW⟩2.0.CO;2

Tiedtke, M. 1989, Monthly Weather Review, 117, 1779, doi: 10.1175/1520-0493(1989)117⟨1779: ACMFSF⟩2.0.CO;2

Tokano, T. 2017, Icarus, 289, 120,
doi: https://doi.org/10.1016/j.icarus.2017.02.005

Tokano, T., McKay, C. P., Neubauer, F. M., et al. 2006,
Nature, 442, 432, doi: 10.1038/nature04948

Tomasko, M., Bézard, B., Doose, L., et al. 2008, Planetary
and Space Science, 56, 648,
doi: https://doi.org/10.1016/j.pss.2007.10.012

Turtle, E. P., Del Genio, A. D., Barbara, J. M., et al.
2011a, Geophysical Research Letters, 38,
doi: 10.1029/2010GL046266

Turtle, E. P., Perry, J. E., Hayes, A. G., et al. 2011b,
Science, 331, 1414, doi: 10.1126/science.1201063

Wolf, E., & Toon, O. 2013, Astrobiology, 13, 656,
doi: 10.1089/ast.2012.0936

Wolf, E. T., & Toon, O. B. 2015, Journal of Geophysical
Research: Atmospheres, 120, 5775,
doi: 10.1002/2015JD023302

Wordsworth, R. D., & Pierrehumbert, R. T. 2013,
Astrophysical Journal, 778,
doi: 10.1088/0004-637X/778/2/154

Yang, D., & Seidel, S. D. 2020, Journal of Climate, 33, 2841
, doi: https://doi.org/10.1175/JCLI-D-19-0260.1

Yano, J.-I., & Plant, R. S. 2012, Reviews of Geophysics, 50,
doi: https://doi.org/10.1029/2011RG000378

Zhang, G., & McFarlane, N. A. 1995, Atmosphere-Ocean,
33, 407, doi: 10.1080/07055900.1995.9649539

APPENDIX

A. LIST OF PHYSICAL SYMBOLS, CONSTANTS, AND ACRONYMS

Symbol	Definition	Earth-like	Titan-like
a	Bulk-plume parameter		
A_u, A_d	Horizontal area of updrafts and downdrafts (m^2)		
B	Buoyancy (m s^{-2})		
B_u, B_d	Buoyancy of updrafts and downdrafts (m s^{-2})		
c	Condensation rate in convective updrafts (kg m^{-3}s^{-1})		
c_{va}	Isochoric specific heat of dry air (J kg^{-1}K^{-1})	719	707.2
c_{vv}	Isochoric specific heat of the condensable gas (J kg^{-1}K^{-1})	1418	1707.4
c_{vl}	Isochoric specific heat of the condensable liquid (J kg^{-1}K^{-1})	4119	3381.55
c_{vs}	Isochoric specific heat of the condensable solid (J kg^{-1}K^{-1})		
c_p	Isobaric specific heat of air (J kg^{-1}K^{-1})		
$c_{pa} = c_{va} + R_a$	Isobaric specific heat of dry air (J kg^{-1}K^{-1})	1006.04	1004.
$c_{pv} = c_{vv} + R_v$	Isobaric specific heat of the condensable gas(J kg^{-1}K^{-1})	1879	2225.68
$\Delta(c_p T) + \Delta(gz)$	Dry static energy difference between the sub-cloud and cloud layer (J kg^{-1})		
CAPE	Convective available potential energy (J kg^{-1})		
CIN	Convective inhibition (J kg^{-1})		
$\dot{D}$	Rate of dissipation (W)		
d	Convective detrainment rate (kg m^{-3}s^{-1})		
e	Convective entrainment rate (kg m^{-3}s^{-1})		
e^*	Saturation vapor pressure of the condensable (Pa)		
f	Frictional force per unit mass (m s^{-2})		
$\tilde{F}_a$	Spatially-resolved net radiative flux from the atmosphere (W m^{-2})		
E_{0v}	Specific internal energy difference between condensable gas and liquid at T_{trip} (J kg^{-1})	2.374×10^6	4.9×10^5
E_{0s}	Specific internal energy difference between condensable liquid and solid at T_{trip} (J kg^{-1})	3.34×10^5	5.86×10^4
F_a	Net radiative flux from the atmosphere (W m^{-2})		
$F_{a,sc}$	Net radiative flux from sub-cloud layer (W m^{-2})		
$F_{a,cl}$	Net radiative flux from the cloud layer (W m^{-2})		
$\tilde{F}_s$	Spatially-resolved net radiative flux at the surface (W m^{-2})		
F_s	Net radiative flux at the surface (W m^{-2})		
g	Gravitational acceleration (m s^{-2})	9.81	1.35
h or MSE	Moist static energy (J kg^{-1})		
h_{sc}	Moist static energy of the sub-cloud layer (J kg^{-1})		
h_{cl}	Moist static energy of the cloud layer (J kg^{-1})		
Δh	Moist static energy difference between the sub-cloud and cloud layer (J kg^{-1})		
h^*	Saturation moist static energy (J kg^{-1})		
L	Latent heat of vaporization of the condensable (J kg^{-1})	2.5×10^6	5.5×10^5
$\Delta(Lq)$	Latent energy difference between the sub-cloud and cloud layer (J kg^{-1})		
LCL	Lifting condensation level		
LFC	Level of free convection		
LNB	Level of neutral buoyancy		
LTRH	Lower-tropospheric radiative heating		
M	Convective mass flux (kg m^{-2}s^{-1})		
$M \times B$	Buoyancy flux (W m^{-3})		
M_{sc}	Sub-cloud mass flux (kg m^{-2}s^{-1})		
M_u, M_d	Mass flux of updrafts and downdrafts (kg m^{-2}s^{-1})		

Symbol	Description		
$M_{u,sc}$	Updraft mass flux in the sub-cloud layer (kg m^{-2}s^{-1})		
$M_{d,cl}$	Downdraft mass flux in the cloud layer (kg m^{-2}s^{-1})		
PE	Precipitation efficiency		
p	Total atmospheric pressure (Pa)		
p_{trip}	Triple point pressure (Pa)	611.65	11700.
P_s	Surface precipitation rate (kg m^{-2}s^{-1})		
q	Specific humidity (kg kg^{-1})		
q^*	Saturation specific humidity (kg kg^{-1})		
$\tilde{Q}_a$	Spatially-resolved atmospheric cooling rate per unit mass (W kg^{-1})		
Q_a	Atmospheric cooling rate (W)		
Q_s	Surface heating rate (W)		
QE	Quasi-equilibrium		
R_a	Specific gas constant of dry air (J kg^{-1}K^{-1})	287.04	296.8
R_v	Specific gas constant of the condensable gas (J kg^{-1}K^{-1})	461	518.28
RH	Relative humidity		
RO	Relaxation oscillator		
s	Specific entropy (J kg^{-1}K^{-1})		
$\dot{s}_d$	Spatially-resolved specific entropy change due to frictional dissipation (W kg^{-1}K^{-1})		
$\dot{s}_{rad}$	Spatially-resolved specific entropy change due to radiative processes (W kg^{-1}K^{-1}		
S	Entropy (J K^{-1})		
$\dot{S}_d$	Entropy change due to frictional dissipation (W K^{-1})		
$\dot{S}_{irr}$	Entropy change due to irreversible processes (W K^{-1})		
$\dot{S}_{rad}$	Entropy change due to radiative processes (W K^{-1})		
$\Delta\dot{S}$	Entropy change due to all irreversible processes except frictional dissipation (W K^{-1})		
SI	Vertically-integrated sink of condesable gas from phase changes (kg m^{-2}s^{-1})		
T	Spatially-resolved atmospheric temperature (e.g., parcel/plume) (K)		
$\overline{T}$	Time- and horizontally-averaged temperature (K)		
T_a	Mean temperature at which atmospheric radiation is emitted (K)		
$1/T_a$	Mean inverse temperature at which atmospheric radiation is emitted (K^{-1})		
T_d	Mean temperature at which frictional dissipation occurs (K)		
T_s	Surface temperature (K)		
T_{trp}	Tropopause temperature (K)	200	71
T_{trip}	Triple point temperature (K)	273.16	90.68
v	Air velocity (m s^{-1})		
V	Volume (m^3)		
$\dot{W}$	Rate of work (W)		
δ	Fractional detrainment efficiency (m^{-1})		
ε	Fractional entrainment efficiency (m^{-1})		
η	Efficiency of the convective heat engine		
η_{max}	Maximum efficiency of the convective heat engine		
γ	Moisture lapse rate (kg kg^{-1}m^{-1})		
Γ	Temperature lapse rate (K m^{-1})		
ρ	Spatially-resolved density of air (e.g., plume/parcel) (kg m^{-3})		
$\overline{\rho}$	Time- and horizontally-averaged density (kg m^{-3})		

B. DIAGNOSIS OF CONVECTIVE PARAMETERS: RESULTS AND INTERPRETATION

Figure 8 shows the mean temperature at which radiation is emitted from the atmosphere T_a, the precipitation efficiency PE, the mean tropospheric relative humidity RH, and the bulk-plume parameter a, as diagnosed from the

convection-resolving simulations of Seeley & Wordsworth (2021a) and the ECHAM6 single-column model. Below, we discuss important trends and inter-model differences.

First, we consider the inter-model differences in PE (Figure 8b,f). Besides its relevance to the hydrological cycle, we care about PE because it allows us to diagnose a. The trend in PE with surface temperature in the convection-resolving model is not reproduced by the single-column model. In the convection-resolving model, PE takes values between 5-30%. The PE in the single-column model is substantially larger at all surface temperatures (up to a factor of 10). To understand why, we diagnose the precipitation efficiencies of the large-scale and convection schemes in the single-column model separately. The convective and large-scale precipitation efficiencies are $PE^u = P_s^u/SI^u$ and $PE^{ls} = P_s^{ls}/SI^{ls}$ (see also Section 4.1.7). Note that these quantities are not strictly additive (i.e., they do not sum to PE). These separate metrics for precipitation efficiency, gross condensation, and surface precipitation are shown in Figure 9. Figure 9b reveals that there are two condensation regimes. For surface temperatures below 325 K, the majority of gross condensation in the atmosphere is convective in origin (Figure 9b). For this reason, PE is biased towards PE^u below 325 K (Figure 9a). Above 325 K, the fraction of gross condensation in updrafts decreases while the fraction of gross condensation in the large-scale environment increases, until the two are roughly equal in magnitude at 335 K (Figure 9b). Large-scale and convective sources of precipitation are displayed in Figure 9c, demonstrating that the latter dominates the total precipitation at every surface temperature. The bias of surface precipitation to the convection scheme is a well-documented behavior of general circulation models (Chen et al. 2021). Total surface precipitation is curtailed above 320 K (Figure 9c) as a result of the water vapor window closing and shortwave absorption increasing, which is a robust phenomenon in hothouse climates (Liu et al. 2024). Comparing the separate sources of gross condensation and surface precipitation, it is clear that the convection scheme is significantly more efficient than the large-scale scheme. Consistent with this interpretation, PE^u ranges from 50-100% and PE^{ls} is at most a few percent (Figure 9a). Lastly, there is a gradual decrease in PE between 325 to 350 K (Figure 9a). Figure 9b,c demonstrates that this decrease is related to the increasing fraction of gross condensation originating in the large-scale scheme, which biases the PE towards PE^{ls}.

Why is the convection scheme so much more efficient than the large-scale scheme in the single-column model? The answer lies in the parameterization design. In the convection scheme, a fraction of the condensates produced in updrafts are converted into convective precipitation. The rest is detrained into the environment, and is then converted into
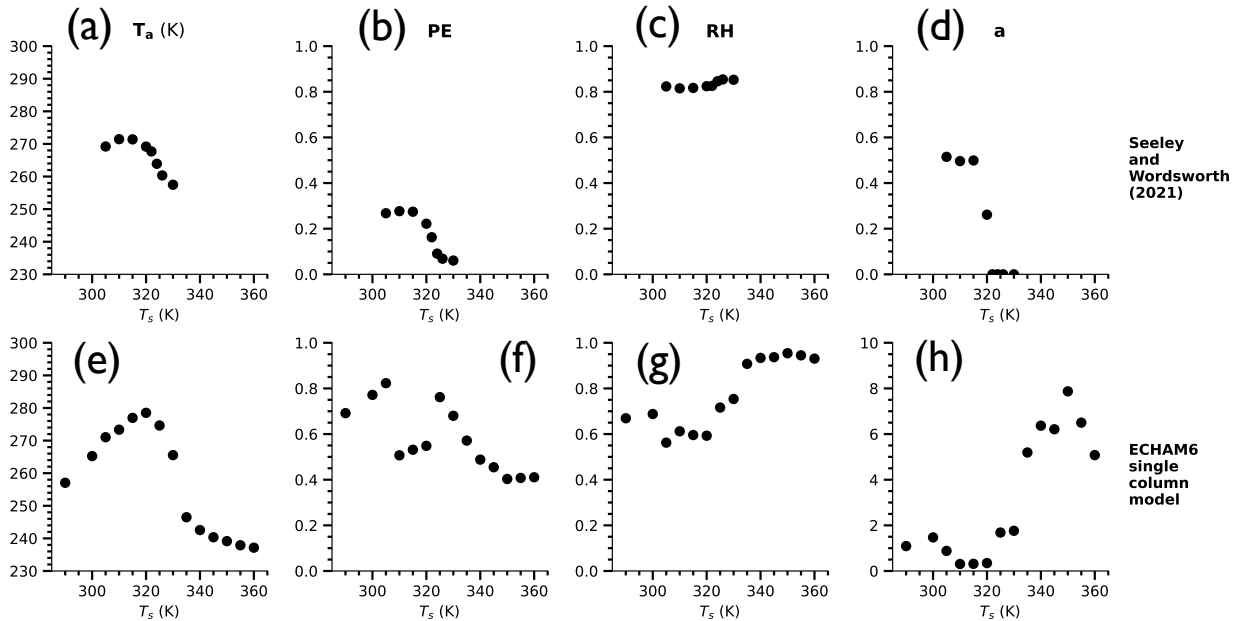

Figure 8. As a function of surface temperature, (a,e) mean temperature at which radiation is emitted, T_a, (b,f) precipitation efficiency PE, (c,g) mean tropospheric relative humidity RH, and (d,h) bulk-plume parameter a from simulations with (a–d) a convection-resolving model (Seeley & Wordsworth 2021a) and (e–h) the ECHAM6 single-column model.
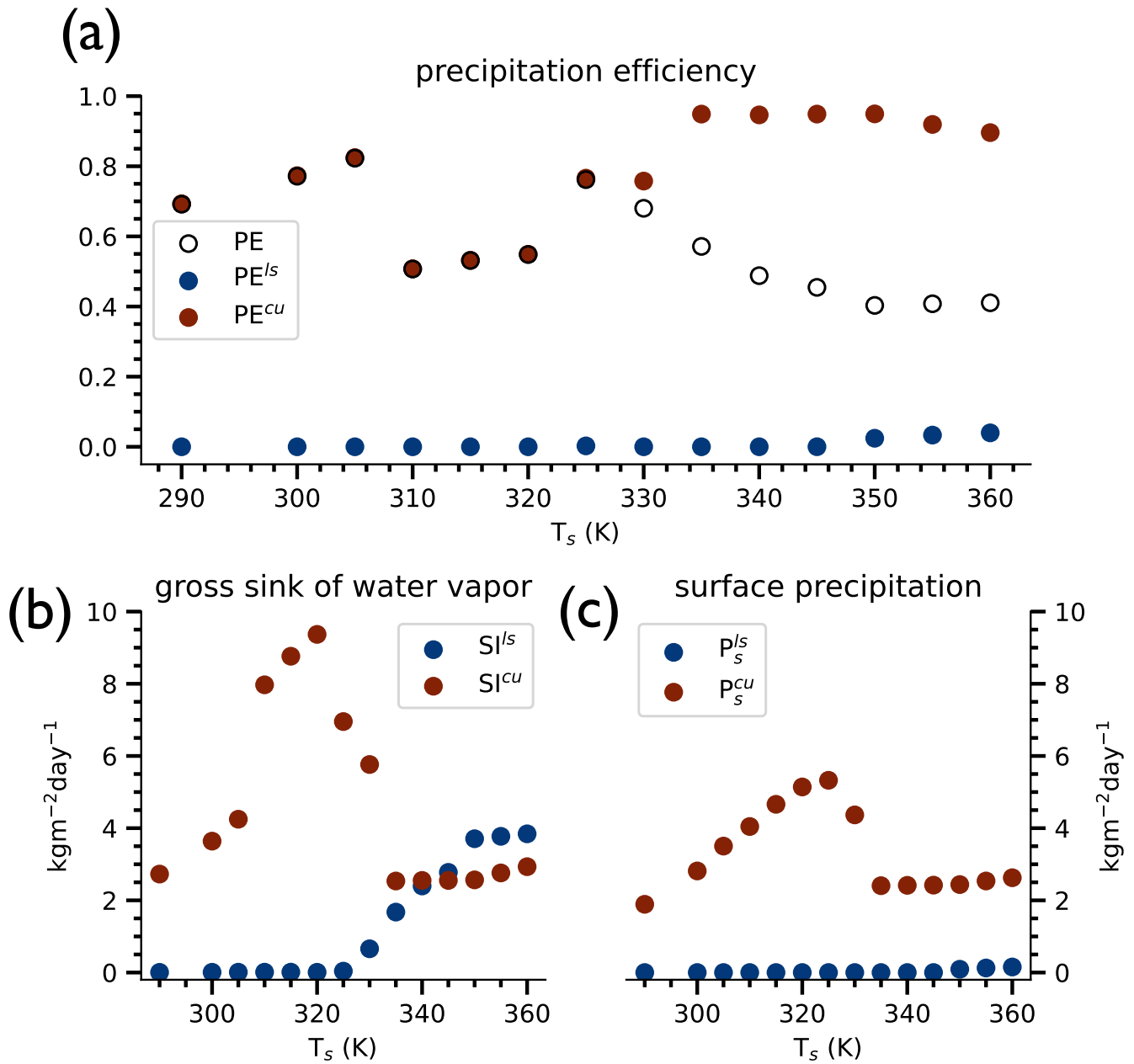
Figure 9. Diagnosed quantities from the ECHAM6 single-column model. (a) PE compared to the precipitation efficiency of the large-scale scheme PE^{ls} and the convection scheme PE^{u}. For visual clarity, PE is an unfilled marker. (b) Vertically-integrated gross sink of water vapor due to phase changes in the large-scale scheme SI^{ls} and the convection scheme SI^{u}. (c) Surface precipitation from the large-scale scheme P_s^{ls} and the convection scheme P_s^{u}.

stratiform clouds or large-scale precipitation by the large-scale scheme. The large-scale precipitation is re-evaporated as it descends through the sub-saturated environment, but the convective precipitation is *assumed* to fall through the saturated updraft (this precludes re-evaporation of convective precipitation in the middle troposphere) and exits from the updraft base near the surface. This "insulation" of convective precipitation from environmental conditions within the plumes supports the persistent near-surface drizzle. In contrast, large-scale precipitation is exposed to sub-saturated environmental conditions during descent, which could explain why the overwhelming majority of gross

condensates are re-evaporated before reaching the surface (Figure 9c). The difference in PE between the schemes is likely due to these assumptions. The convection-resolving model simulations tell us that the real PE should be closer to that of the large-scale scheme at high surface temperatures (Figures 8f and 9a). It might be possible to tune our model to have a lower PE at high temperatures in accordance with the convection-resolving simulations. We leave this as a future task, as the bias in the partitioning of rainwater in climate models is widespread (Chen et al. 2021) and beyond the scope of our work.

Using the PE (Figure 8b,f) and mean tropospheric RH from the simulations (Figure 8c,g), we are able to diagnose the bulk-plume parameter in both models. a is found to be less than 0.5 in the convection-resolving simulations on account of the high RH and low PE (Figure 8b,c). In the context of the zero-buoyancy theory (Section 2.2), this means that convective plumes and environmental air are moderately coupled. a is substantially larger in the single-column model; it ranges from 0.3-1.5 below 325 K and from 1.5-8 above 325 K (Figure 8h). There is a significant increase in a above 325 K (Figure 8h) related to the decline in PE, rather than the increase in RH (the latter would act to reduce a). Figure 10 shows the effect of varying a between 0.5-8 on the theoretical CAPE. In general, larger values of a support more steady-state storage of CAPE (e.g., Figure 10a). Low values of a give a better fit to the convection-resolving model simulations (Figure 10a), as might be expected from Figure 8d. Conversely, $a = 8$ yields values for CAPE that approach those observed at high surface temperatures in the single-column model (Figure 10b).

Interestingly, the theoretical temperature of QE breakdown is sensitive to the value of a (Figure 10b). We are interested in this sensitivity as a potential explanation for the 30 K difference in the surface temperature of RO emergence between the models. As you increase a, the temperature of QE breakdown decreases (Figure 10b). Why is this? The dry static energy has a strong dependence on a in the theory because of the location of the minimum in tropospheric MSE. In the zero-buoyancy theory, decreasing a reduces the lapse rate, which causes the MSE minimum to rise to a higher elevation. This means that the dry static energy difference becomes more negative (and therefore reduces Δh) with decreasing a. That a is larger in the single-column model does not seem to explain why the RO state emerges at a lower surface temperature in the convection-resolving model.

However, the theoretical prediction for QE breakdown is sensitive to the method of estimating vertical heat transport. In this study, we chose to use a simple difference of the MSE between the surface and the tropospheric minimum value. Consider the scenario in Figure 10a where Δh is approximated by the latent energy $\Delta(Lq)$. In this case where we have neglected the vertical dry static energy difference, the temperature of QE breakdown is instead found to *increase*
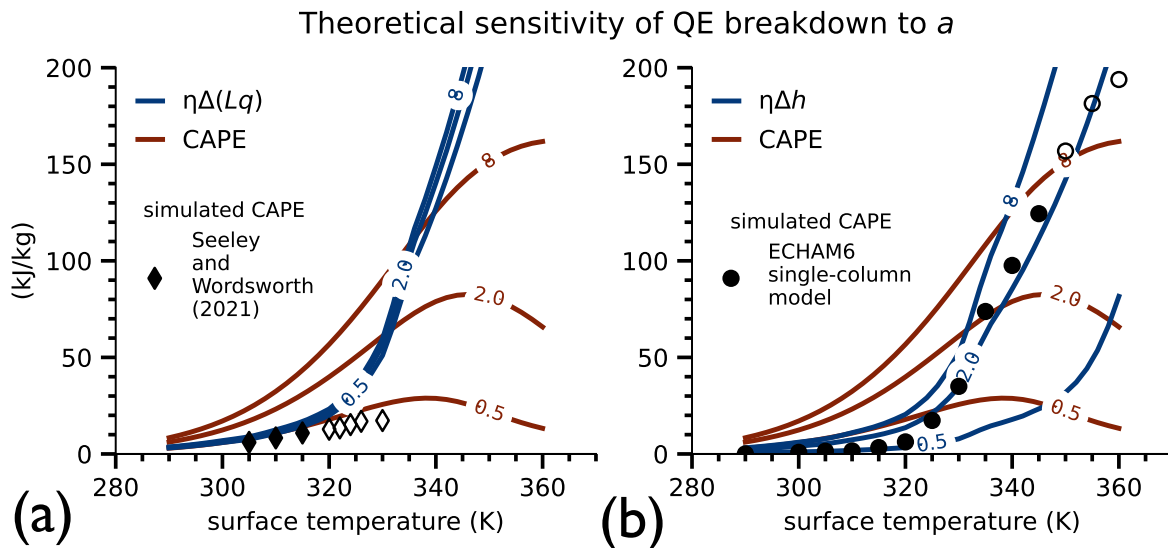

Figure 10. Theoretical sensitivity of the QE breakdown hypothesis to varying the bulk-plume parameter a. The (solid) theoretical profiles are labeled by values of a between 0.5 and 8. We initialize the parcel at an assumed pressure of 1 bar, the temperature of the surface, and PE=25%. In (a), we estimate the vertical heat transport as the vertical latent energy difference $\Delta(Lq)$ only. The simulated CAPE from Seeley & Wordsworth (2021a) is plotted for reference (symbols). In (b), we estimate the vertical heat transport as the vertical moist static energy difference Δh. The simulated CAPE from the single-column model is plotted for reference. As in the main text, filled markers indicate QE states and unfilled markers indicate RO states.

with increasing a. This result is more consistent with our intuition, and leads us to suspect that there is a better way to estimate the vertical heat transport. Future work should therefore interrogate our assumptions about the vertical heat transport in an atmosphere with zero buoyancy. We assumed that upward air records the MSE near the surface and downward air records the minimum in MSE, but is that consistent with zero buoyancy? The environmental temperature and moisture profile in the zero-buoyancy model is a reflection of the mutual interaction (entrainment, detrainment, re-evaporation) between ascending and descending air. In this process, air parcels exchanged across the same level have the same dry static energy, and differ only in their moisture content. This might mean that the appropriate measure of vertical heat transport in the zero-buoyancy atmosphere is not Δh, but rather $\Delta(Lq)$ or some variant thereof.

C. HOW TO CALCULATE CAPE IN THE SIMULATIONS

This appendix summarizes our process of calculating CAPE in the simulations (Romps 2008, 2015; Marquet 2016; Emanuel 1994). To ensure consistency in our analysis, we apply the same parcel methods to the data from the convection-resolving model of Seeley & Wordsworth (2021a) and our single-column model. The values of thermodynamic constants for Earth-like and Titan-like atmospheres are given in Appendix A.

Moist air is defined to be a mixture containing dry air and a condensable in various phases. The mass fraction (i.e. specific humidity) is represented by the symbol q_x. x is a generic subscript referring either to dry air a, condensable gas v, condensable liquid l, or condensable solid s. The mixing ratio is represented by the symbol r_x, and is related to the specific humidity by $r_x = q_x/q_a$. The density of dry air is $\rho_a = p_a/(R_aT)$. The partial pressure of dry air in the parcel is a function of the total pressure p (given by the simulation) and the mixing ratio of the condensable gas r_v:

$$p_a = p(1 + r_v/\epsilon)^{-1}, \tag{C1}$$

where $\epsilon = R_a/R_v$. When the specific volume of liquid and solid phases of the condensable are neglected, the density of the moist air parcel is (Emanuel 1994)

$$\rho = \frac{p}{R_aT}\frac{1 + r_t}{1 + r_v/\epsilon}, \tag{C2}$$

where $r_t = r_v + r_l + r_s$ is the total mixing ratio of the condensable. For simplicity, we will ignore the solid phase ($r_s, q_s = 0$) in our parcel calculations and assume that, regardless of temperature, the condensable exists only in the gas and/or the liquid phase; however, we will retain variables associated with ice in subsequent equations for reader clarity. The saturation vapor pressure over liquid is (Romps 2008, 2015)

$$e^{*,l} = p_{trip}\left(\frac{T}{T_{trip}}\right)^{(c_{pv}-c_{vl})/R_v} \times \exp\left[\frac{E_{0v} - (c_{vv} - c_{vl})T_{trip}}{R_v}\left(\frac{1}{T_{trip}} - \frac{1}{T}\right)\right], \tag{C3}$$

where p_{trip} and T_{trip} are the triple point pressure and temperature, c_{pv} is the isobaric specific heat of condensable gas (J kg^{-1} K^{-1}), c_{vv} and c_{vl} are the isochoric specific heats of condensable gas and condensable liquid (J kg^{-1} K^{-1}), and E_{0v} is the difference in specific internal energy between condensable gas and condensable liquid at the triple point temperature (J kg^{-1}; Romps 2015). The saturation specific humidity over liquid is then given by

$$q^{*,l} = \frac{\rho_v^*}{\rho} = \frac{R_a}{R_v}\frac{e^{*,l}}{p}\frac{1 + r_v/\epsilon}{1 + r_t} \tag{C4}$$

To determine the lapse rate of an "adiabatic parcel"[16], we invoke the conservation of the sum of MSE and CAPE (Marquet 2016; Romps 2015): that is, MSE + CAPE. Taking the vertical derivative of this conserved quantity and using the definition of CAPE,

$$\frac{\partial \text{MSE}}{\partial z} = -\frac{\partial}{\partial z}\int_{\text{LFC}}^{z} B(z')\, dz' = -B(z) \tag{C5}$$

where

$$\text{MSE} = [q_a c_{pa} + (q_v + q_l + q_s)c_{vl}](T - T_{trip}) + q_v L_c - q_s L_f + gz. \tag{C6}$$

---

[16] Here, "adiabatic" refers to any parcel that is raised without exchanging heat or mass with its surroundings, irrespective of the assumptions about moisture removal in the lifting method. For pseudo-adiabatic ascent, we remove all moisture after each discrete lifting step. For reversible ascent, the total moisture is conserved over the entire ascent.

c_{pa} is the isobaric specific heat of dry air (J kg^{-1} K^{-1}), $L_c = E_{0v} + R_v T + (c_{vv} - c_{vl})(T - T_{trip})$ is the latent heat of condensation (J kg^{-1}), and $L_f = E_{0s} + (c_{vl} - c_{vs})(T - T_{trip})$ is the latent heat of fusion (Jkg^{-1}). c_{vs} is the isochoric specific heat of condensable solid (J kg^{-1} K^{-1}), and E_{0s} is the difference in specific internal energy between condensable liquid and condensable solid at the triple point temperature (J kg^{-1}; Romps 2015).

For detailed instructions on how to obtain the temperature and density profile of an adiabatic parcel with the same pressure as the local environment using conservation of MSE+CAPE, we refer the reader to Romps (2015). However, we do offer a short summary below. MSE and B at height z depend on T and q_x. The MSE at $z + \Delta z$ follows from Equation C5. Solving for the parcel temperature at $z + \Delta z$ from the MSE (Equation C6) requires a root solver. The reason is that MSE is a function of both temperature and the condensable mass fraction, where the partitioning between vapor, liquid, and solid phases is itself temperature-dependent. The solution constraints are that the vapor phase must remain pegged to the saturation value above the LCL and total moisture must be conserved during each discrete lifting step. When the level of neutral buoyancy is reached, the buoyancy $B(z)$ can be integrated upward from the LFC to yield CAPE.

We have thus far detailed the parcel method for reversible ascent, where the total moisture in the parcel is conserved. We now discuss how to approach lifting scenarios where total moisture is not conserved, such as pseudo-adiabatic ascent.

C.1. *Ascent with condensate removal*

An example of irreversible ascent is where the condensed liquid or solid in the parcel is removed in part or in whole (i.e., pseudo-adiabatic). This process usually carries away a small amount of mass. The changing mass of the parcel produces a change in the specific humidity, which is accounted for as follows. The initial mass of the parcel is $m_{tot}^i = m_a^i + m_v^i + m_l^i + m_s^i$. The superscripts i and f are used to track the initial and final state of the parcel. For simplicity, we only detail the treatment of liquid removal, but note that ice removal would proceed analogously. Condensate removal is parameterized as exponential decay following Seeley & Wordsworth (2023):

$$\frac{\partial q_l}{\partial z} = -q_l/L, \tag{C7}$$

where L is a characteristic length scale. Suppose that we remove a mass of condensable liquid $\Delta m_l < 0$ as prescribed by Equation C7. The final and initial masses are related by $m_a^i = m_a^f$, $m_v^i = m_v^f$, and $m_l^f = m_l^i + \Delta m_l$, where we have neglected ice. The final mass fraction for dry gas and condensable gas are

$$q_a^f = \frac{m_a}{m_{tot}^i + \Delta m_l} = \frac{q_a^i}{1 + \Delta q_l} \text{ and } q_v^f = \frac{m_v}{m_{tot}^i + \Delta m_l} = \frac{q_v^i}{1 + \Delta q_l}, \tag{C8}$$

where in the second step we divided through by m_{tot}^i. The liquid removal step increases the mass fraction of dry gas and vapor in the parcel by a factor of $(1 + \Delta q_l)^{-1}$. The final mass fraction for condensable liquid is

$$q_l^f = \frac{m_l^f}{m_{tot}^f} = \frac{m_l^i + \Delta m_l}{m_{tot}^i + \Delta m_l} = \frac{q_l^i + \Delta q_l}{1 + \Delta q_l}, \tag{C9}$$

where we have accounted for the changing total mass in addition to the total mass of condensable liquid. This method can be used to evaluate lifting processes from fully reversible ($L \to \infty$) to pseudo-adiabatic ($L \to 0$). The final mass fractions are used to update the parcel buoyancy and MSE before the next discrete lifting step.